**NASA
Technical
Paper
3041**

1990

On-Orbit Structural Dynamic Performance of a 15-Meter Microwave Radiometer Antenna

Deborah M. Wahls
and Jeffery T. Farmer
Langley Research Center
Hampton, Virginia

David W. Sleight
University of Illinois
Urbana, Illinois

Summary

Analyses were conducted to determine the performance of a low-frequency microwave radiometer located on a geostationary platform subject to representative onboard disturbances. Parameter limits on antenna performance were defined for the root-mean-square surface roughness, pointing error, and defocus. The antenna concept and science requirements were defined, and a finite-element model was generated. A subreflector scanning scenario was developed and corresponding input excitation functions were modeled to represent the onboard disturbances to the system consisting of a 30-min Earth-disk scan with a 10-km footprint. A modal analysis was performed on the antenna for two configurations: free-flying and planform-mounted. The resulting mode shapes and natural frequencies were input to the forced-response analysis, which was performed for each configuration with the defined scanning disturbance. The forced-response analysis then quantified the dynamic distortions and their impact on the performance parameters was assessed. The distortions in the surface contributed to all three errors, the displacement of the subreflector added to the pointing error and defocus, and the displacement of the vertex was a component of the defocus.

The results of this analysis show that the strong-back and feed mast of the low-frequency microwave radiometer (LFMR) as designed are capable of maintaining their shapes within specifications for the assumed on-orbit disturbance, particularly in the platform-mounted configuration which exhibited errors within their respective limits by at least an order of magnitude. This was also true for the free-flyer surface roughness and defocus; however, the free-flyer maximum pointing error was significantly closer to, yet still within, its specified limit.

Introduction

The Mission to Planet Earth is a proposed NASA program (ref. 1) to monitor and study the Earth's hydrologic, biogeochemical, and climate cycles on a global scale. The type of observations to be made include various surface, atmospheric, and oceanic changes that occur in the global Earth system because of both environmental and man-made conditions. These fluctuations must be quantified and analyzed in terms of their interaction with humanity; the resulting data will be instrumental in forecasting future global system events. NASA is proposing technology development programs to produce both the sensors to perform the necessary observations and the spacecraft and data handling technologies required to support these instruments.

The complement of spacecraft needed to support the desired observations will consist of low-inclination low Earth orbit (LEO), polar LEO, and geosynchronous Earth orbit (GEO) platforms, each carrying a payload of instruments and sensors. Each of the three types of platforms will provide an observation environment that is best suited for its specific instruments. The LEO platforms will provide low temporal resolution, high spatial resolution, and global coverage, whereas the GEO platforms will provide improved temporal resolution and nearly hemispherical coverage but with reduced spatial resolution.

The study presented in this paper addresses the structural dynamic performance of a large antenna concept aboard a proposed geostationary platform. The sequence of analyses employed here may be applied to a wide range of on-orbit assessments of reflector antennas. A list of instruments and the proposed concept used here for the geostationary platform is described in reference 2. The platform configuration, illustrated in figure 1, is a NASA Langley Research Center (LaRC) concept, derived from that of reference 3.

The geostationary platform concept supports 18 different scientific instruments with widely diverse requirements while providing a stiff, stable platform environment for pointing accuracy. Most of these instruments are relatively small compared with the platform, except for two large reflector antennas: the 7.5-m-diameter high-frequency microwave sounder (HFMS) and the 15-m-diameter low-frequency microwave radiometer (LFMR). These two antennas are a significant part of the structural configuration and could greatly impact the dynamic behavior of the platform. Each antenna was analyzed individually in terms of its structural behavior and its ability to perform within the operating constraints of the system. A discussion of the thermal structural behavior of the high-accuracy HFMS primary reflector is documented in reference 4, whereas the present paper addresses the structural dynamic behavior of the 15-m-diameter LFMR subject to a representative on-orbit disturbance. The large aperture and focal length of the LFMR make it the more flexible of the two antennas and therefore more susceptible to performance degradation caused by on-orbit dynamic disturbances.

In this study, an antenna structure for the LFMR is proposed based upon existing technology that should meet the mass and volume constraints of the transportation system (as determined in presently unpublished data by J. L. Garrison and L. F. Rowell of the Langley Research Center). This paper discusses the antenna structural modeling and the

modeling of the excitation functions used to represent a potential on-orbit dynamic disturbance, i.e., subreflector scanning. Two configurations are used for the analyses, and these are described along with their corresponding mode shapes and natural vibration frequencies. The forced-response analysis is reported in terms of the impact of the subreflector scanning on the following antenna geometric performance parameters: reflector surface roughness, pointing error, and defocus. Each of these parameters is a contributing factor to electromagnetic performance degradation of antennas.

Although the LFMR is a receiver antenna, this paper occasionally refers to its "emitted beam." It should be noted that this is done for clarity in the explanation of various aspects of the performance of the antenna, which is the same for an emitter as for a receiver.

Symbols

D	diameter of primary reflector, m
F	subsatellite footprint diameter, km
f	focal length, m
f/D	ratio of focal length to diameter
f_ℓ	frequency of line scans, Hz
f_n	natural vibration frequency, Hz
H	orbit altitude, km
I	mass moment of inertia, kg-m^2
I_{xx}, I_{yy}, I_{zz}	mass moments of inertia about x-, y-, and z-axes, respectively, kg-m^2
I_{xy}, I_{yz}, I_{zx}	mass products of inertia with respect to reference planes, kg-m^2
M	moment, N-m
M_x	north-south input torque, N-m
$M_{x,\text{reset}}$	north-south input torque for reset maneuver, N-m
M_y	east-west input torque, N-m
t	time as measured from beginning of a line scan, sec
t_ℓ	time for east-west line scan, sec
t_S	time for north-south step-down procedure, sec
t_{TA}	time for turnaround procedure, sec
x, y, z	coordinate axes as defined in figure 1

θ_x	north-south angular displacement, deg
$\theta_{x,\text{reset}}$	north-south angular displacement for reset maneuver, deg
λ	wavelength of operating frequency, m
$\Phi_{f,x}$	pointing error about x-axis due to feed/subreflector displacement, rad
$\Phi_{f,y}$	pointing error about y-axis due to feed/subreflector displacement, rad
$\Phi_{s,x}$	pointing error about x-axis due to surface distortion, rad
$\Phi_{s,y}$	pointing error about y-axis due to surface distortion, rad
Φ_t	total pointing error, rad
Φ_x	combined pointing error about x-axis, rad
Φ_y	combined pointing error about y-axis, rad
$\dot{\omega}$	angular acceleration, rad/sec^2
ω_x	north-south angular velocity, deg/sec
$\dot{\omega}_x$	north-south angular acceleration, deg/sec^2
$\omega_{x,\text{max}}$	maximum north-south angular velocity, deg/sec
$\omega_{x,\text{reset}}$	north-south angular velocity for reset maneuver, deg/sec
$\dot{\omega}_{x,\text{reset}}$	north-south angular acceleration for reset maneuver, deg/sec^2
ω_y	east-west angular velocity, deg/sec
$\dot{\omega}_y$	east-west angular acceleration, deg/sec^2
$\omega_{y,av}$	average east-west scan rate (angular velocity) of subreflector, deg/sec
$\omega_{y,\text{beam}}$	average east-west scan rate (angular velocity) of emitted beam, deg/sec

Abbreviations and acronyms:

DOF	degrees of freedom
FEM	finite-element model
GEO	geosynchronous Earth orbit
HFMS	high-frequency microwave sounder
LASS	Large Advanced Space Structures

LEO   low Earth orbit

LFMR   low-frequency microwave radiometer

PSR   Precision Segmented Reflector

rms   root mean square

SDRC   Structural Dynamics Research
               Corporation

TTSS   Tetrahedral Truss Structural
               Synthesizer

LFMR Design and Structural Model

The LFMR must operate at frequencies of 6, 10, 18, 21, and 37 GHz (ref. 5) to meet the science requirements for the various measurements it will make. It will monitor precipitation at frequencies of 18, 21, and 37 GHz, and observations of snow will be conducted at 18 and 37 GHz. The ocean will be observed at frequencies of 6, 10, and 18 GHz to measure surface temperature, surface wind, wind vector curl, surface geostrophic currents, and the motion of high wind patterns. Sea ice will be monitored at 10, 18, and 37 GHz.

The 15-m-diameter LFMR configuration used in this study is illustrated in figure 2. Its reflector is offset fed so as to avoid blockage of the signal by the feed system. Cassegrain geometry is used so that scanning may be performed by rotating a subreflector rather than the feed system and its associated waveguides. A high effective ratio of focal length to diameter (f/D) of 1.5 is needed to retain accuracy during scanning maneuvers. The geometry of the LFMR, illustrated in figure 3, is dictated by these factors as well as the geometry of the geostationary platform (ref. 2). The relative sizes of the various LFMR components were selected consistent with an effort to minimize overall antenna mass and to avoid blocking the view of either the other instruments or the LFMR itself. All this yields a system consisting of a paraboloidal primary reflector with an extended feed mast that supports a subreflector and an electronic feed system. A mass summary of these components is shown in table 1, and the finite-element model (FEM) is shown in figure 4. A description of the main structural components of the LFMR follows.

Primary Reflector

The primary reflector is a 15-m-diameter, offset-fed paraboloid with its edge offset from the vertex of the parent paraboloid by 3 m, as shown in figure 3. It consists of a tetrahedral truss structure (referred to here as a "strongback") supporting a membrane reflector surface. The membrane, made of 0.5-mil-thick aluminized Du Pont Kapton (1.42 g/cm^3), is attached to the strongback at each of the strongback top-surface joints. An assumption is made that no "pillowing" of the membrane surface exists between the connection points, which implies the use of additional tie cords between the strongback joints and the membrane. The tetrahedral truss strongback provides a stiff, stable support for the membrane surface to minimize the distortion of the overall reflector shape.

The truss configuration selected for this study is that of the General Dynamics GEOTRUSS (ref. 6), which is a 12-bay truss composed of graphite/epoxy composite tube members with aluminum alloy joints and end fittings. It was selected for this configuration because of its advanced level of development and its lightweight, high-strength characteristics. The physical and material properties of the truss tube elements are listed in table 2.

The primary reflector portion of the FEM shown in figure 4 consists of 235 nodes, 954 beam elements, and 362 lumped mass elements (not shown). Each node represents the location of a strongback joint and supports a lumped mass element representing the mass of the appropriate joint and end fittings. Each node on the reflector side (top surface) of the strongback supports an additional lumped mass element representing the appropriate portion of the membrane distributed mass. The beam elements connecting the nodes represent the strut tubes of the strongback truss.

Feed Mast

The feed mast used for this analysis is based on the Minimast truss (ref. 7) developed at LaRC as a ground test article to characterize the structural behavior and control of large space structures. It is used in this study because of its known structural characteristics. The Minimast is a deployable, retractable, triangular linear truss constructed of graphite/epoxy composite tubes with aluminum alloy hinges and end fittings. The LFMR feed mast (illustrated in fig. 2) attaches to the reflector strongback at one end and supports the subreflector 19.5 m above the vertex of the parent paraboloid at the other end and the feed system 17.5 m above the vertex of the parent paraboloid. (See fig. 3.)

An equivalent beam structural model of the Minimast was developed for use in this study to reduce the number of degrees of freedom (DOF) in the already complex LFMR model. The physical and material properties of the equivalent beam structural model are shown in table 3. The feed mast model is composed of 18 beam elements (each representing a bay

of Minimast truss) and 19 nodes (each supporting a lumped mass element representing the appropriate mass and torsional inertia of the hinges and connectors between each truss bay). The mast is connected to the primary reflector via three rigid bars (indicated by "R" in fig. 4).

Subreflector

The subreflector size, which was determined from Cassegrain antenna geometry, was based on the following: (1) the height of the subreflector above the primary reflector in the direction of the primary-reflector parent-paraboloid axis of symmetry (19.5 m), and (2) the offset distance of the primary reflector from the vertex of its parent paraboloid (fig. 3). The resulting subreflector was determined to be 2.35 m in diameter. Since a high-precision subreflector surface will be required for the operating frequencies of the LFMR, the surface was assumed to be constructed of solid panel segments supported by a tetrahedral truss strongback, similar to those under current study as a part of the Precision Segmented Reflector (PSR) program (ref. 8). An areal density of 12 kg/m^2 was assumed for the panels and strongback, resulting in a subreflector mass of 52 kg.

For the structural model, the subreflector is approximated as a single mass element concentrated at a single node with its inertias computed as for a right circular cylinder with the above dimensions and mass. It is attached to the feed mast via a rigid bar connection (indicated by "R" in fig. 4) at 19.5 m above the vertex of the parent paraboloid.

Feed System

Since the details of the feed system design are not yet known, approximate calculations were used to determine a representative feed system for incorporation in the LFMR model. The mass of the feed system is estimated based on that of the scanning feed array of a single-aperture Earth-sensing radiometer feed system described in reference 9. This estimate, described by Garrison and Rowell, yields a feed mass of 443 kg. Like the subreflector, the feed array is represented as a lumped mass in the structural model of the antenna system. It is rigidly connected to the feed mast at 17.5 m above the vertex of the parent paraboloid.

Modal Analysis

A description of the software used to perform the modal analyses is included in the appendix. Preliminary modal analyses were first performed on the reflector alone and the feed beam alone to serve

as a comparison with the complete antenna system. These were performed with free-free (unrestrained) boundary conditions resulting in fundamental frequencies of 14.06 and 2.18 Hz, respectively. The LFMR was then analyzed in two configurations, the free-flyer antenna and the platform-mounted antenna, as follows.

Free-Flyer Antenna

It has been suggested that the LFMR be flown aboard its own dedicated spacecraft because of its large size and mass. The complete antenna was therefore analyzed in a free-free configuration to simulate orbiting the LFMR as a free flyer (i.e., on a dedicated spacecraft) with the assumption that the supporting subsystem masses are negligible compared with the mass of the antenna.

Use of the flexible feed mast to attach the massive subreflector and feed system to the more massive primary reflector dramatically lowers the structural frequencies of the overall antenna system from that of either the reflector or the feed mast alone. The rigid connection between the dish and feed mast acts to cantilever the mast to the reflector, thus resulting in the lower fundamental frequency of 1.38 Hz for the overall system, which corresponds to a feed mast bending mode shape as expected. Figures 5-13 illustrate the first nine mode shapes for the free-flyer antenna, and table 4 lists their corresponding natural frequencies along with a brief description of each mode shape. For clarity, the distortions are greatly exaggerated and only the elements that comprise the strongback top surface (where the membrane is attached), the feed mast, and the rigid bar connector to the subreflector are shown in all mode shape figures. Both the mode shapes (solid lines) and the undeformed geometries (dashed lines) are shown.

In general, the free-flying configuration has mode shapes that exhibit rotation of both the feed beam and the reflector about the point where they are rigidly connected. An inspection of the lower flexible body mode shapes suggests that modes 2 and 3 are most likely to contribute to pointing errors about the x-axis. Pointing errors about the y-axis include modes 1 and 4. The mode shapes that may contribute to the defocus of the antenna include modes 1 and 4. Contributions may also be made by higher-order modes; however, these will be less significant than those of the lower-order modes. Surface-accuracy errors, however, are probably induced by combinations of all the dynamic modes, since they all exhibit distortions to the optimum paraboloidal shape, with the lower-order modes being the primary contributors.

Platform-Mounted Antenna

Next, the antenna was rigidly attached at three central nodes on the bottom of the strongback to the geostationary platform, which is represented as a lumped mass with appropriate mass properties as listed in table 5. (See fig. 4.) This platform-mounted configuration was also analyzed under free-free conditions. In this configuration the effects of the mass and inertia of the platform are considered but not its dynamic characteristics. The resulting natural frequencies and mode shape descriptions are listed in table 6, with the mode shapes being illustrated in figures 14–22. Connecting the LFMR to the considerably greater mass and inertia of the platform lumped mass acts to nearly cantilever the entire antenna at the connection region, thus yielding a structure with natural frequencies much lower than those of the free-flyer case.

The mode shapes seen for this case appear somewhat similar to those of the free-flyer case. The rigid connection of the reflector and the platform mass, coupled with the relatively large inertia of the platform about the y-axis (see fig. 1), yields a cantilever-like condition about the y-axis for the entire antenna system. This causes several general differences between the corresponding mode shapes of the two configurations, which are discussed below.

The three nodes attached to the platform mass tend to remain relatively fixed, particularly about the y-axis, which is the axis of greatest platform inertia. In general, the pointing errors about the y-axis due to the distortion of the surface are therefore expected to be less for the platform-mounted configuration than for the free-flyer configuration. Nearly fixing these three nodes also causes the reflector to move about its own center, i.e., the area of connection to the platform mass, rather than to move about the connection to the feed mast, as was seen in the free-flyer case.

An inspection of the mode shapes indicates that modes 2 and 4 are probably the lower-order modes that contribute to pointing errors about the x-axis. The y-axis pointing error modes include modes 1 and 3. Those that may contribute to the defocus of the antenna include modes 1 and 3. As in the free-flyer case, surface roughness errors appear to be induced by combinations of all the dynamic modes, particularly the lower-order modes.

On-Orbit Dynamic Disturbances and Excitation Functions

From its location in geosynchronous orbit, the LFMR will need to scan most of the Earth disk, although the exact scanning operation is undecided at this time. There are a variety of alternatives being examined, including mechanical scanning, electronic scanning, and combinations thereof. This study assumes that the scanning will be accomplished mechanically, without momentum compensation (for conservatism), by rotating the subreflector about its x- and y-axes for north-south and east-west scanning, respectively. The subreflector motion is one of the primary on-orbit disturbances that could degrade the electromagnetic performance of the antenna by inducing surface roughness, pointing errors, and defocus. A representative onboard disturbance that simulates subreflector scanning was modeled to evaluate the dynamic performance of the LFMR in space. This disturbance consists of two torque input equations representing the orthogonal components of the scan (i.e., subreflector rotation about the x- and y-axes).

Excitation (torque) functions were generated for a representative scanning scenario based on the retrace time (the time allotted for each Earth-disk scan) and the footprint (the projection of the half-power beamwidth on the Earth) requirements. More frequent retraces yield more severe forcing conditions, since the subreflector must be rotated more quickly. Smaller footprints also cause quicker movements and higher accelerations since there are more spots to scan within the allotted retrace time. The retrace time examined was 30 min (1800 sec), which is appropriate for a range of proposed science requirements.

The Earth footprint capabilities of the LFMR were found using the following equation (ref. 5):

$$F = H(1.2\lambda/D)$$

where F is the subsatellite footprint diameter, H is the orbit altitude ($H_{GEO} = 35\,760$ km), λ is the wavelength of the operating frequency, and D is the diameter of the antenna primary reflector. The resulting footprints for the various operating frequencies of the 15-m-diameter LFMR are listed in table 7. In order to provide a conservative disturbance model, this study assumes a 10-km footprint for the 30-min retrace time, which may better satisfy the science requirements and is more stringent than the values in table 7.

The LFMR was assumed to employ a raster-type scan technique. A raster scan involves dividing the desired area into a grid of spots with dimensions of the desired resolution and then scanning back and forth line by line across the grid. As shown in figure 23, the scenario for the LFMR assumes that a line is scanned from east to west, followed by a north-south step down to the succeeding line, which is then scanned from west to east. This "S" pattern

is repeated until the entire area is scanned. The following discussion describes the formulation of the torque functions for the subreflector raster scan.

From geosynchronous orbit, the coverage requirement of $\pm 7.3°$ from nadir (ref. 10) yields an area of the Earth disk of approximately 9160×9160 km. The required 10-km ground resolution required therefore results in 916 lines of 916 footsteps each (10×10 km per footstep). The 30-min allotted time is assumed for operational scanning, i.e., not including time for a reset maneuver or for damping out its associated vibrations. The time to scan each line t_ℓ, including turnaround, is therefore the retrace time divided by the number of lines and is given as follows:

$$t_\ell = 1800 \text{ sec}/916 \text{ lines}$$

$$= 1.965 \text{ sec/line}$$

The time for line scan t_ℓ occurs between points B and F in figure 23. Note that the frequency of the line scans ($f_\ell = 1/t_\ell$) is 0.509 Hz, which is quite close to the first fundamental frequency of the platform-mounted configuration (0.45 Hz). Operating near a resonant condition increases the conservative nature of the scan disturbance model.

East-West Scan

The average east-west scan rate of the beam $\omega_{y,\text{beam}}$ is

$$\omega_{y,\text{beam}} = \frac{14.6 \text{ deg/line}}{1.965 \text{ sec/line}}$$

$$= 7.430 \text{ deg/sec}$$

Because of the Cassegrain configuration, the beam emitted by the antenna is displaced twice the angle of the subreflector rotation. The required subreflector average scan rate is therefore

$$\omega_{y,\text{av}} = 7.431/2$$

$$= 3.716 \text{ deg/sec}$$

which is the scan rate assumed for the steady east-west portion of each scan line.

The time for turnaround t_{TA} is assumed to be 10 percent of the total line time. (In fig. 23, $t_{TA} = 0.1965$ sec from point B to point E.) During this time, the subreflector must decelerate about the y-axis from $\omega_y = 3.716$ deg/sec to zero, displace a north-south step about the y-axis, and accelerate about the y-axis in the negative direction to $\omega_y = -3.716$ deg/sec. The angular velocity about

the y-axis of the turnaround maneuver is assumed to be a cosine wave of the following form:

$$\omega_y = 3.716[\cos(\pi t/0.1965)] \text{ deg/sec}$$

The magnitude of the acceleration function is

$$\dot{\omega}_y = 59.416[\sin(\pi t/0.1965)] \text{ deg/sec}^2$$

The corresponding torque disturbance function is therefore

$$M_y = 18.623[\sin(\pi t/0.1965)] \text{ N-m} \qquad (1)$$

(where $M = I\dot{\omega}$, $I_{xx} = I_{yy} = 18$ kg-m^2, and degrees are converted to radians).

As defined here, each line of scan begins with $t = 0$ sec at the beginning of a turnaround maneuver (point B in fig. 23). The transient torque equation is therefore in effect during each line for the time segment 0 sec $\leq t \leq 0.1965$ sec (fig. 23, point B through point E). There is no east-west torque input while the east-west velocity is a constant ($\omega_y = 3.716$ deg/sec or $\omega_y = -3.716$ deg/sec, as appropriate), which occurs during the rest of the line scan ($0.1965 \leq t \leq 1.965$, point E to point F). This torque function is applied alternately in the positive and negative sense to simulate the velocities and accelerations due to the back-and-forth east-west motion. The east-west excitation function is plotted in figure 24(a).

North-South Step

The north-south step time t_S is assumed to be 25 percent of the turnaround time ($t_S = 0.0491$ sec). The step occurs from point C to point D in figure 23. During this time the subreflector must accelerate about the x-axis from $\omega_x = 0$ deg/sec to some value of $\omega_{x,\text{max}}$, and then decelerate back to zero. With each step the beam must displace the width of one line (10 km), or 0.016°. This requires a subreflector displacement of 0.008°. Adjusting the time so that $t = 0$ sec corresponds with that of the east-west case (i.e., point B of fig. 23), the assumed cosine form displacement equation during the step-down procedure is

$$\theta_x = 0.004\{\cos[\pi(t - 0.0737)/0.0491]\} \text{ deg}$$

The equations of the angular velocity ω_x and acceleration $\dot{\omega}_x$ for the north-south step are, respectively,

$$\omega_x = -0.2562\{\sin[\pi(t - 0.0737)/0.0491]\} \text{ deg/sec}$$

and

$$\dot{\omega}_x = 16.388\{\cos[\pi(t - 0.0737)/0.0491]\} \text{ deg/sec}^2$$

The torque function M_x is therefore

$$M_x = 5.137\{\cos[\pi(t - 0.0737)/0.0491]\} \text{ N-m} \quad (2)$$

The north-south disturbance is always applied in the positive sense during the operational scan to facilitate the progression of the scan from the northernmost line to the southernmost line. The transient torque equation for the north-south motion is in effect during the time period $0.0737 \text{ sec} \le t \le 0.1228 \text{ sec}$ (fig. 23, point C to point D), whereas the north-south displacement θ_x and therefore the input torque M_x are zero during the rest of the line scan: $0 \text{ sec} \le t \le 0.0737 \text{ sec}$ (point B to point C) and $0.1228 \text{ sec} \le t \le 1.965 \text{ sec}$ (point D to point F). The function is applied concurrently with the east-west function. The north-south function is plotted in figure 24(b).

Reset Maneuver

A representative 15 lines of scan were found to be sufficient to quantify the dynamic behavior of the antenna. Along with the 15 lines of operational scan, a nonoperational reset maneuver is modeled and incorporated into the analysis. The purpose of this maneuver is to reset the subreflector from its position at the end of an Earth-disk scan (fig. 23, point G) to its proper position to begin the next Earth-disk scan (fig. 23, point A). Since no measurements are made during this maneuver, the reset also serves as an indicator to the data recorders of the end of one Earth-disk scan and the beginning of the next. This study assumes that the reset maneuver takes the same amount of time as one line of scan (t_ℓ). This diagonal maneuver is broken down into its orthogonal components below.

East-west component. The east-west component of the reset maneuver is modeled simply as another line of scan. The moment input function to begin the reset is merely a negative cosine pulse identical in magnitude to that of equation (1), whereas the input to end the reset and begin the next Earth-disk scan is a positive pulse of equation (1).

North-south component. The modeling of the north-south component of the reset maneuver differs from that of the east-west component in several ways. The north-south angular velocity component immediately prior to the reset is $\omega_x = 0$ deg/sec, unlike

the east-west angular velocity component which is $\omega_y = -3.716$ deg/sec. Therefore, the north-south reset pulse component does not need to first decelerate the subreflector to zero as does the east-west component. Also, the overall geometry of the antenna and the geostationary platform must be considered. Care must be taken to avoid excessive torque inputs about the x-axis, since this is the axis about which there is least inertia. (See fig. 1.) Consequently, extreme torques about this axis are likely to induce excessive rocking about the x-axis.

The north-south component is therefore assumed to be a single large "step" from the southernmost line back up to the northernmost line, modeled in a manner similar to the individual north-south steps of the operational scan. This manner of north-south reset results in a low-acceleration motion of the subreflector throughout the 1.965 sec of the maneuver, unlike the east-west reset which is composed of a relatively large acceleration pulse followed by a long period of zero-acceleration coasting. The north-south reset component is formulated as follows:

$$\theta_{x,\text{reset}} = -7.3\{\cos[\pi(t - 0.0737)/1.965]\} \text{ deg}$$

$$\omega_{x,\text{reset}} = 11.671\{\sin[\pi(t - 0.737)/1.965]\} \text{ deg/sec}$$

$$\dot{\omega}_{x,\text{reset}} = -18.659\{\cos[\pi(t - 0.737)/1.965]\} \text{ deg/sec}^2$$

$$M_{x,\text{reset}} = -5.862\{\cos[\pi(t - 0.737)/1.965]\} \text{ N-m}$$

Note that $M_{x,\text{reset}}$ must be applied in the negative direction to bring the subreflector from the southernmost line back to the northernmost line. The north-south reset component pulse is less severe than that of the east-west component since the velocity changes slowly over the course of the entire reset maneuver, rather than changing quickly at the beginning of the line and then coasting for the rest of it. The input to begin the first line of the next Earth-disk scan is then simply a pulse equal to equation (2).

Antenna Structural Analysis

A static analysis of the LFMR has been made by L. F. Rowell and G. D. Qualls of the Langley Research Center in presently unpublished data. The dynamic performance analysis of the LFMR in the present paper consists of using the natural frequencies and corresponding mode shapes of each configuration as determined by the modal analysis, along with the torque inputs from the subreflector scan, to perform a forced-response analysis. The resulting dynamic displacements are then used to quantify the antenna geometric errors. The LFMR performance is evaluated in terms of the effect that the surface

node distortions have on the rms surface roughness, pointing error, and defocus, as well as in terms of the effect that the subreflector displacement has on the pointing error and defocus. A description of the software used to perform the various analyses is given in the appendix.

Geometric Performance Criteria

The electromagnetic performance of an antenna can be adversely affected by numerous factors. Among these is the geometric displacement of the various structural components of the antenna from their optimum positions. Minimizing the overall surface roughness, pointing error, and defocus is of extreme importance for high-precision reflector antennas such as the LFMR.

Surface roughness. The surface roughness of a reflector antenna is defined as the root mean square (rms) of the reflector surface distortions relative to the best-fit paraboloid through the distorted surface locations. The maximum allowable rms surface roughness for an antenna can generally be related to both the wavelength λ of its highest operating frequency and to its application. For Earth-scanning radiometer systems such as the LFMR, the allowable rms error has been specified to be within the range from $\lambda/50$ to $\lambda/100$ (refs. 10 and 11, respectively). The $\lambda/100$ limit was used for this analysis to provide the more conservative requirement. The 37-GHz LFMR operating frequency therefore has a maximum allowable rms error of 8.11×10^{-5} m (3.2 mils).

Pointing error. In the present study, the pointing error of a reflector antenna consists of two parts: the angular rocking of the primary reflector and the physical displacement of the feed mast. Angular rocking is defined as the rotation of the best-fit paraboloid relative to the original undistorted paraboloid and is referred to here as "the pointing error due to surface distortion." Feed mast displacement contributes to the pointing error because displacing the feed and/or subreflector laterally from their optimum positions with respect to the Cassegrain geometry repoints the emitted beam. For the present LFMR configuration, the subreflector and feed are sufficiently close for their relative displacements to be considered negligible. The subreflector contribution to the pointing error is therefore calculated as the change in the angle that the subreflector makes with the axis of symmetry of the undistorted paraboloid (i.e., the z-axis).

The combination of these pointing errors is illustrated in figure 25. As the figure shows, the combined pointing error about the x-axis Φ_x is as follows:

$$\Phi_x = 2\Phi_{s,x} - \Phi_{f,x} \tag{3}$$

where $\Phi_{s,x}$ is the pointing error due to the surface distortion (i.e., angular rocking of the primary reflector) and $\Phi_{f,x}$ is the pointing error due to the subreflector (i.e., feed mast) displacement. Similarly, about the y-axis,

$$\Phi_y = 2\Phi_{s,y} - \Phi_{f,y} \tag{4}$$

The magnitude of the total LFMR pointing error Φ_t is equal to the angle between the pointing direction of the distorted antenna and the optimum pointing direction (the axis of symmetry of the undistorted paraboloid) and is found by

$$\Phi_t = \cos^{-1}(\cos\Phi_x \cos\Phi_y) \tag{5}$$

The maximum allowable pointing error for the LFMR was assumed to be 10 percent of the beamwidth (ref. 6), and, like the surface roughness, the pointing error is dependent on the highest operating frequency. The pointing error limit is 6.22×10^{-5} rad (12.83 arcsec).

An additonal factor that may contribute to the total antenna pointing error is the redirection of the subreflector caused by localized bending of the feed mast. Since the mechanism by which the subreflector will be connected to the mast has not yet been determined, this issue is not addressed in detail in the present study, which assumes that a rigid connection exists between the subreflector and feed mast.

Defocus. The defocus of an antenna consists of three parts: the difference between the focal length of the best-fit paraboloid and that of the undistorted reflector, the translation of the feed/subreflector along the axis of symmetry, and the translation of the paraboloid vertex along the axis of symmetry. The total defocus in this first-order analysis is defined as the linear sum of these three factors. The maximum allowable defocus has been identified in the range from 0.2 to 2.0 times the wavelength of the highest operating frequency (ref. 6). Using the more conservative requirement of 0.2λ yields a defocus limit of 1.62×10^{-3} m (63.9 mils).

Analysis Procedure

For each LFMR configuration, dynamic displacement data were calculated based on the input disturbance functions in the three translational DOF at a representative set of top-surface nodes (where

8

the membrane is attached) as well as at the single subreflector node. The displacement data were then evaluated as to their effect on the optimum LFMR shape.

The subreflector displacement data were evaluated as previously described. The surface node displacement data were used in conjunction with the Utku-Schmele best-fit paraboloid technique (ref. 12) to quantify the antenna performance in terms of its rms surface roughness, pointing error, and defocus. The Utku-Schmele technique calculates the geometric properties of the undistorted paraboloid reflecting surface, as well as those of a new paraboloid which most closely fits through the distorted surface node positions. The rms error is then calculated based on the displacement of the distorted nodes from the best-fit paraboloid. The pointing error and defocus are quantified by comparing the new best-fit paraboloid axis of symmetry, focus, and vertex with those of the original, undistorted paraboloid. The pointing error is output as the angular rocking of the dish about the x- and y-axes. The defocus results are given as the difference in the focal lengths of the distorted and undistorted paraboloids and the translation of the vertex in the focal direction.

Results

The resulting dynamic error curves are shown in figures 26–31 for the free-flyer antenna and in figures 32–37 for the platform-mounted antenna. Several general comments about these curves are given below, followed by specific descriptions of the individual error curves that are summarized in table 8. Identification of specific modal contributions to the various errors is performed by close visual inspection of their cyclic trends and supported by fast Fourier transform analysis (ref. 13) of the error curves. For the pointing error and defocus curves, primary modal contributions are readily identified; however, specific modal contributions to the rms curves cannot be distinguished. Instead, the primary frequency contributing to the rms response appears to be the line frequency of the scan input ($f_\ell = 0.509$ Hz), as evidenced by the sharp peaks in the rms curves that occur at 1.965-sec intervals. These peaks are also evident in the x-axis pointing error curves. For clarity, the error curves show the first 25 sec of response. The effect of the reset is not shown since it was found to have minimal impact on the errors, increasing the magnitude of the x-axis pointing errors only. After the reset is completed, each of the errors continues to oscillate, eventually damping out to zero. In no case does the reset maneuver induce errors that are outside the specified limits.

Free-Flyer Antenna

Surface roughness. The rms surface roughness for the free-flyer antenna is shown in figure 26. The rms error reaches a local maximum value at the time of application of each input torque, i.e., at approximately t_ℓ intervals, and then begins to damp out until the subsequent torque is applied. The entire curve is well within the rms limit of 8.11×10^{-5} m, with its maximum magnitudes approximately 5.3×10^{-6} m.

Pointing error. The pointing error about the x-axis is shown in figures 27(a) and (b) for the surface and subreflector contributions, respectively, and in figure 27(c) for the combined error about the x-axis, as determined by equation (3). These curves show insignificant errors during the scan input, with a maximum combined pointing error around 1.2×10^{-6} rad. As was seen in the rms curve, the maximum values in each of the three curves occur at the points of application of the input torques, and each maximum is followed by a damping motion until the next torque is applied. The combined curve exhibits behavior from modes 2, 3, and 5 (figs. 6, 7, and 9, respectively). Each of these contributing modes is an x-axis rocking-dominated mode. The pointing error about the y-axis is shown in figures 28(a) for the surface contribution, 28(b) for the subreflector contribution, and 28(c) for the combined pointing error from equation (4). The combined-error curve has a maximum value of 1.9×10^{-5} rad and has the frequency of the first free-free mode (fig. 5), which is a rocking about the y-axis by both the surface and the subreflector.

The total LFMR pointing error for the free-flyer antenna as determined by equation (5) is shown in figure 29. Note that this curve is a measure of the magnitude of the pointing error, not its direction. Torque application points are again seen as local maxima that damp out until the subsequent torque is applied. The maximum free-flyer pointing error is about 1.9×10^{-5} rad, which occurs primarily about the y-axis. This is well within the allowable 6.2×10^{-5} rad limit.

Defocus. Figures 30(a), (b), and (c) show the surface, subreflector, and vertex defocus curves, respectively, with maximum defocus values of 5.8×10^{-5}, 4.7×10^{-5}, and 5.2×10^{-5} m, respectively. The sum of these curves is shown in figure 31 and remains within the required limit of 1.62×10^{-3} m with a maximum defocus of 1.3×10^{-4} m. This curve shows a low-frequency response dominated by mode 1 (fig. 5), which includes a curling and flattening motion in the dish and a movement of the subreflector both toward and from the dish surface.

9

Platform-Mounted Antenna

Surface roughness. The rms surface roughness for the platform-mounted configuration is plotted in figure 32 and is well within the specified rms limit with a maximum of about 4.7×10^{-6} m. As in the free-flyer case, the points of the input disturbances are the points of maximum rms error. These errors then damp out during the steady-motion portion of the subreflector scan and again spike to maximum values at the next turnaround.

Pointing error. Figures 33(a), (b), and (c) illustrate the pointing error about the x-axis caused by the surface, subreflector, and combined displacements, respectively. The combined curve in figure 33(c) has a maximum value of 2.7×10^{-6} rad, and it exhibits mode 2 and mode 7 behavior. The curves exhibit a reaction at the point of application of the torque similar to that of the free-flyer case. The pointing error increases to a local maximum and then damps down until the next torque is applied. The subreflector curve in figure 33(b), however, exhibits an additional response: the application of the torque appears to excite higher frequency modes that damp out quickly before the subsequent excitation occurs. The pointing error about the y-axis is shown in figures 34(a), (b), and (c) for the surface, subreflector, and combined distortions, respectively. The combined response is shaped by modes 1 and 3 (figs. 14 and 16) for the surface curve and has a maximum value of 4.5×10^{-6} rad.

The total pointing error from equation (5) for the platform-mounted LFMR is shown in figure 35. Again, there are local maxima at the torque application points that damp out until the subsequent torque input. The maximum platform-mounted pointing error is approximately 4.5×10^{-6} rad, which is about one-fourth that of the free-flyer configuration because of the cantileverlike connection to the platform, which has a large inertia about the y-axis relative to the x-axis. This connection inhibits rotation about the y-axis which, for both the free-flyer and platform-mounted configurations, is the primary contribution to the total pointing error. Therefore, the total pointing error is lower for the platform-mounted configuration than for the free-flyer configuration.

Defocus. The defocus curves are plotted in figures 36(a), (b), and (c), respectively, for the surface, subreflector, and vertex defocus errors with maximum magnitudes of 7.0×10^{-5}, 2.4×10^{-5}, and 2.6×10^{-5} m, respectively. The total defocus is plotted in figure 37 with a maximum total error of 7.0×10^{-5}. This curve has both high- and low-frequency characteristics exhibiting mode 1 and mode 8 behavior and remains well within the defocus limit of 1.62×10^{-3} m. The platform-mounted defocus is much smaller than the free-flyer defocus, again because of the cantileverlike connection to the platform mass that causes the reflector to remain relatively fixed and bend about the platform connection region.

Concluding Remarks

Analyses were conducted to determine the performance of a low-frequency microwave radiometer located on a geostationary platform subject to representative onboard disturbances. Parameter limits on antenna performance were defined for the root-mean-square surface roughness, pointing error, and defocus. The antenna concept and science requirements were defined and a finite-element model was generated. A subreflector scanning scenario was developed and corresponding input excitation functions were modeled to represent the onboard disturbances to the system consisting of a 30-min Earth-disk scan with a 10-km footprint. A modal analysis was performed on the antenna for two configurations: free-flying and platform-mounted. The resulting mode shapes and natural frequencies were input to the forced-response analysis, which was performed for each configuration with the defined scanning disturbance. The forced-response analysis then quantified the dynamic distortions and their impact on the performance parameters was assessed. The distortions in the surface contributed to all three errors, the displacement of the subreflector added to the pointing error and defocus, and the displacement of the vertex was a component of the defocus.

The results of this analysis show that the strongback and feed mast of the low-frequency microwave radiometer (LFMR) as designed are capable of maintaining their shapes within specifications for the assumed on-orbit disturbance, particularly in the platform-mounted configuration which exhibited errors within their respective limits by at least an order of magnitude. This was also true for the free-flyer surface roughness and defocus; however, the free-flyer maximum pointing error was significantly closer to, yet still within, its specified limit.

These results indicate that active or passive control techniques may not be necessary for the present LFMR design. It must be noted, however, that these results are based on the assumption of an "ideal" reflector, i.e., that there is no slop in the joints from either manufacturing errors or deployment and that there is no "pillowing" of the membrane reflector surface. Additionally, localized feed mast bending is

not addressed here and may adversely affect overall antenna pointing. Various attachment mechanisms must be examined so as to minimize this effect. The present study also does not include the effects of the geostationary thermal environment, which, in addition to the dynamic disturbance examined here, may cause the errors to exceed the specified limits. Care must be exercised in devising scan scenarios and momentum compensation so as to minimize both the torques that are input to the system due to subreflector rotation and the concurrence of torque input frequencies with the natural frequencies of the system. This includes careful selection of retrace time, footprint size, the details of each line of scan (i.e., the time allotted for turnaround and step-down procedures), and component masses.

Acknowledgment

Appendix

Study Flowchart and Software Description

Figure A1 is a flowchart of this study and indicates the various software used and steps taken. A brief description of each software module and its application to this study follows.

The truss elements of the LFMR tetrahedral truss support were modeled using the Tetrahedral Truss Structural Synthesizer (TTSS) program, which is part of the Large Advanced Space Structures (LASS) program (ref. 14) created by the General Dynamics Corporation. With user-input information such as antenna diameter, number of bays, f/D ratio, structural-element physical and material properties, and hinge and joint specifications, the TTSS program generates mass estimates and finite-element models for use by a structural analysis program.

For the present application, the TTSS finite-element model is transferred to Supertab (ref. 15), which is a part of the I-DEAS software package (ref. 16) developed by the Structural Dynamics Research Corporation (SDRC). This transfer occurs by converting the TTSS output model file to the I-DEAS universal file format and then reading this universal file into Supertab. Supertab is an interactive, menu-driven program used to construct, modify, and visualize finite-element models prior to structural analysis, and to graphically display the results of such an analysis. In Supertab other antenna components (such as the feed beam) were modeled and added to the tetrahedral truss model from LASS.

The structural dynamic behavior of the LFMR was analyzed using the Model Solution program module (ref. 17) of the I-DEAS software, which determined the antenna mode shapes and natural frequencies. Supertab was used for postprocessing and visualizing the mode shapes.

The response of the LFMR to the subreflector scanning was analyzed using the Systan (ref. 18) portion of the I-DEAS software. Systan uses the modal data generated in Model Solution and the user-input forcing functions to calculate the dynamic distortions of the system.

The surface dynamic distortion data were written to an I-DEAS universal file, and the best-fit paraboloid analyses were performed based on these data. The subreflector dynamic displacement data were written to another I-DEAS universal file, and the impacts on the antenna defocus and pointing error were assessed.

```
  ┌─────────┐      ┌──────────────────┐     ┌──────────────────┐     ┌──────────────────────────┐
 │  Define  │     │       TTSS        │    │  Translate model  │    │       Supertab            │
 │   LFMR   │────▶│   Create initial  │───▶│    to I-DEAS       │───▶│ - Read in universal file  │
 │  concept │     │ finite-element    │    │   universal file   │    │ - Modify model as needed  │
 └─────────┘      │      model        │    └──────────────────┘     └──────────────────────────┘
                  └──────────────────┘
```

Define disturbance
excitation functions

| Write I-DEAS universal file of surface distortion data | Systan — Determine response of structure to input disturbances | Model Solution — Determine mode shapes and natural frequencies of structure |

Write I-DEAS universal file of subreflector displacement data

Perform best-fit parabola analysis and plot results

Perform subreflector displacement analysis and plot results

Supertab
- Postprocessing
- Visualization of mode shapes

Figure A1. Study flowchart.

References

1. Ride, Sally K.: *Leadership and America's Future in Space. A Report to the Administrator of NASA*, Aug. 1987.

2. Pidgeon, David Joseph: *A Subsystem Design Study of an Earth Sciences Geostationary Platform.* M.S. Thesis, George Washington Univ., July 1989.

3. Ford Aerospace Corp.: *Geostationary Platform Bus Study for Earth Observation Sciences. Volume II - Comprehensive Report, Final Report*, Sections 1.0 thru 10.0. WDL—TR 11066 (Contract NAS8-36104), Sept. 1987.

4. Farmer, Jeffery T.; Wahls, Deborah M.; and Wright, Robert L.: *Thermal-Distortion Analysis of an Antenna Strongback for Geostationary High-Frequency Microwave Applications.* NASA TP-3016, 1990.

5. Lockheed Missiles & Space Co., Inc.: *Geostationary Platform Study—Contract Extension, Final Report.* LMSC-F278679, Rev. A (Contract NAS8-36103, Modification No. 13, DR-9), Nov. 1988.

6. Dyer, J. E.: *Development of a Verification Program for Deployable Truss Advanced Technology.* NASA CR-181703, 1988.

7. Adams, Louis R.: *Design, Development and Fabrication of a Deployable/Retractable Truss Beam Model for Large Space Structures Application.* NASA CR-178287, 1987.

8. Collins, Timothy J.; and Fichter, W. B.: *Support Trusses for Large Precision Segmented Reflectors: Preliminary Design and Analysis.* NASA TM-101560, 1989.

9. Foldes, Peter: *A Design Study for the Use of a Multiple Aperture Deployable Antenna for Soil Moisture Remote Sensing Satellite Applications.* NASA CR-178154, 1986.

10. Agrawal, Brij N.: *Design of Geosynchronous Spacecraft.* Prentice-Hall, Inc., c.1986.

11. Hedgepeth, John M.: *Structures for Remotely Deployable Precision Antennas—Final Report.* NASA CR-182065, 1989.

12. Ludwig, A., ed.: *Computer Programs for Antenna Feed System Design and Analysis. Volume I: Programs and Sample Cases.* NASA CR-84810, 1967.

13. Clough, Ray W.; and Penzien, Joseph: *Dynamics of Structures.* McGraw-Hill, Inc., c.1975.

14. Leondis, Alex: *Large Advanced Space Systems Computer-Aided Design and Analysis Program—Final Technical Report.* NASA CR-159191-1, 1980.

15. *Supertab®—Engineering Analysis Pre- and Post-Processing User Guide.* I-DEAS™ Level 4, Structural Dynamics Research Corp., c.1988.

16. DeRyder, Leonard J.: Space Station Integrated Computer-Aided Engineering Systems Analysis Software. *NCGA's Computer Graphics '87, Eighth Annual Conference and Exposition—Proceedings, Volume III—Technical Sessions,* National Computer Graphics Assoc., 1987, pp. 249–262.

17. *Supertab®—Engineering Analysis Model Solution and Optimization User Guide.* I-DEAS™ Level 4, Structural Dynamics Research Corp., c.1988.

18. *Systan™—Engineering Analysis System Dynamics User Guide.* I-DEAS™ Level 4, Structural Dynamics Research Corp., c.1988.

Table 1. Mass Summary of Low-Frequency Microwave Radiometer (LFMR)

Component	Mass, kg
Strongback	250
Reflector surface . . .	3
Mast	95
Feed	443
Subreflector	52
Total	843

Table 2. Properties of Strongback Elements

Property	Diagonal elements	Elements for top and bottom surfaces
Young's modulus, N/m^2	1.38×10^{11}	1.38×10^{11}
Poisson's ratio	0.29	0.29
Mass density, kg/m^3	1.52×10^3	1.52×10^3
Cross-sectional area, m^2	3.35×10^{-5}	4.88×10^{-5}
Moment of inertia of cross section, kg-m^2 . . .	1.93×10^{-9}	2.73×10^{-9}
Torsional constant, kg-m^2	3.86×10^{-9}	5.47×10^{-9}
Outer diameter, cm	2.22	2.22
Thickness, mm	0.48	0.70
Average length, m	118.00	150.00

Table 3. Structural Characteristics of Minimast Equivalent Beam Model

Beams:

Axial stiffness, N	1.15×10^8
Bending stiffness, N-m^2	1.22×10^7
Torsional stiffness, N-m^2	1.10×10^6
Mass per unit length, kg/m	4.8

Lumped masses:

	End nodes	Interior nodes
Mass, kg	2.33	2.33
Torsional inertia, kg-m^2	1.48	1.76

Table 4. Natural Frequencies of Free-Flyer LFMR

Flexible mode	Natural frequency, Hz	Description of mode shape
1	1.38	Reflector rocking and mast bending about y-axis
2	2.30	Reflector rocking about x-axis and mast twisting about z-axis
3	2.81	Reflector rocking and mast bending about x-axis
4	7.48	Reflector and mast bending about y-axis
5	9.44	Reflector torsion about x-axis and mast bending about x-axis
6	10.98	Reflector and mast bending about y-axis
7	14.27	Reflector torsion about x-axis and mast bending about x-axis
8	16.65	Reflector torsion about x-axis and mast bending about x-axis
9	18.00	Reflector bending about x-axis and mast bending about y-axis

Table 5. Platform Lumped Mass Properties

Mass, kg 5726

I_{xx}, kg-m^2 . . . . 7.969×10^4

I_{yy}, kg-m^2 . . . . 2.961×10^5

I_{zz}, kg-m^2 . . . . 3.034×10^5

I_{xy}, kg-m^2 . . . . 3.635×10^2

I_{yz}, kg-m^2 . . . . 2.401×10^3

I_{zx}, kg-m^2 . . . . 3.161×10^4

Table 6. Natural Frequencies of Platform-Mounted LFMR

Flexible mode	Natural frequency, Hz	Description of mode shape
1	0.45	Mast bending about y-axis
2	.72	Reflector rocking and mast bending about x-axis
3	2.10	Reflector rocking and mast bending about y-axis
4	2.33	Mast twisting about z-axis
5	6.89	Reflector rocking and mast bending about x-axis
6	7.91	Reflector rocking and mast bending about y-axis
7	8.82	Reflector torsion about x-axis and mast bending about x-axis
8	10.50	Reflector and bending about y-axis
9	13.94	Reflector twisting about z-axis and mast bending about x-axis

Table 7. Footprint Diameter as a Function of Operating Frequency

Operating frequency, GHz	Footprint diameter, km
6	143
10	86
18	48
21	41
37	23

Table 8. Summary of Results

Performance parameter	Assumed limit	Free-flyer		Platform-mounted	
		Maximum	Contributing modes	Maximum	Contributing modes
rms surface roughness, m	8.11×10^{-5}	5.3×10^{-6}	(a)	4.7×10^{-6}	(a)
Pointing error, rad	6.22×10^{-5}	1.9×10^{-5}	2, 3, 5 (x-axis) 1 (y-axis)	4.5×10^{-6}	2, 7 (x-axis) 1, 3 (y-axis)
Defocus, m	1.62×10^{-3}	1.3×10^{-4}	1	7.0×10^{-5}	1, 8

[a]Not applicable.
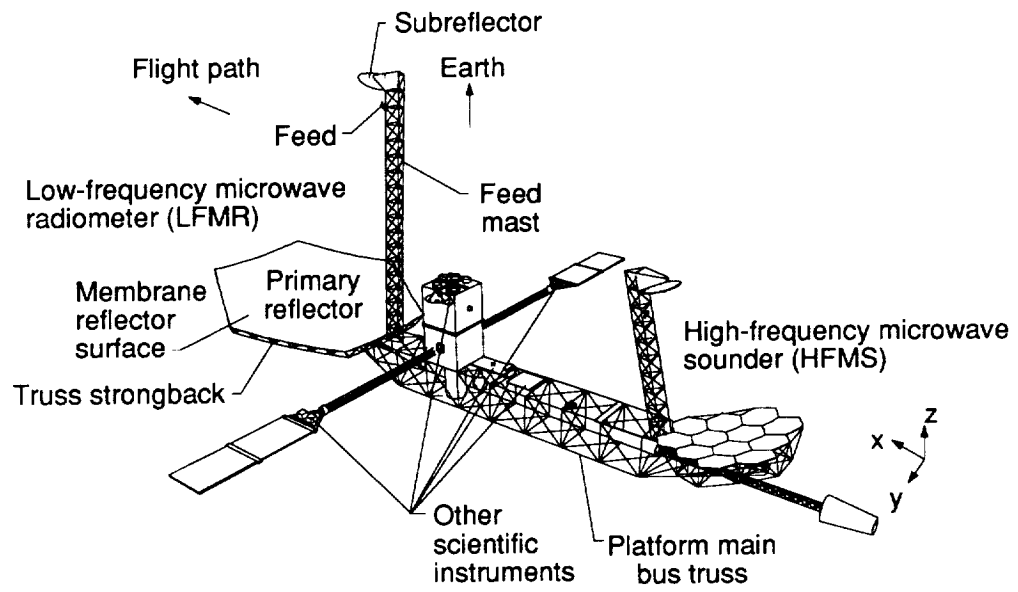
Figure 1. Geostationary Earth-science platform.
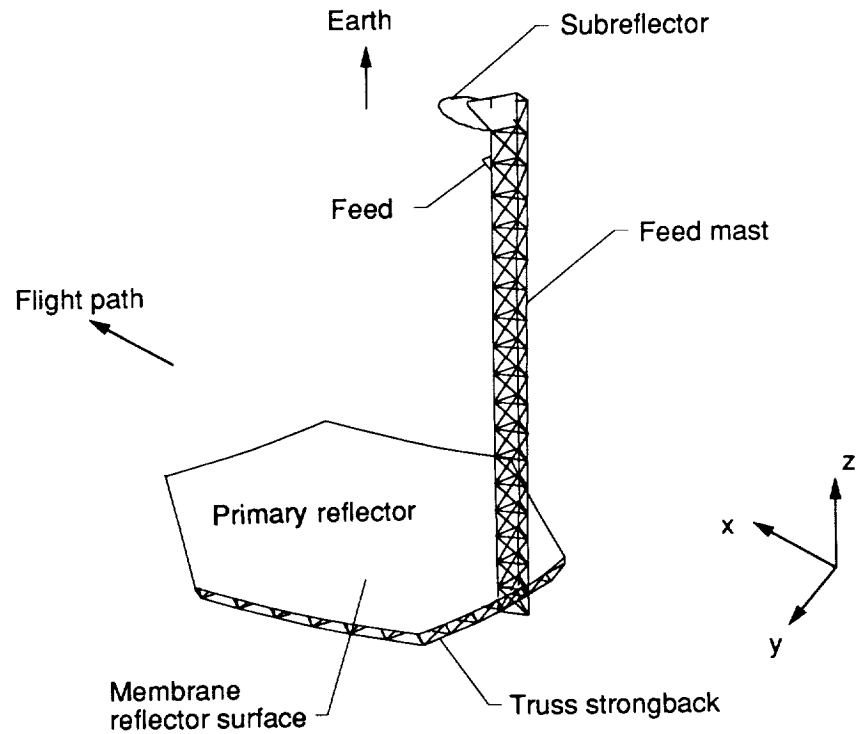
Figure 2. Low-frequency microwave radiometer (LFMR).
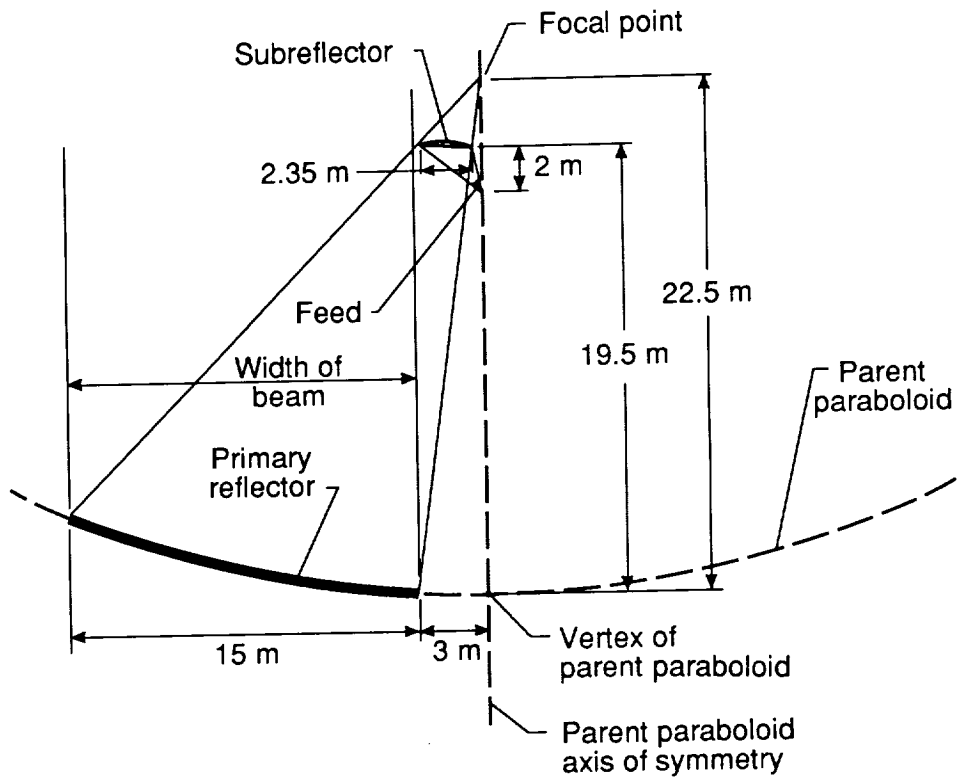
Figure 3. LFMR Cassegrain geometry.
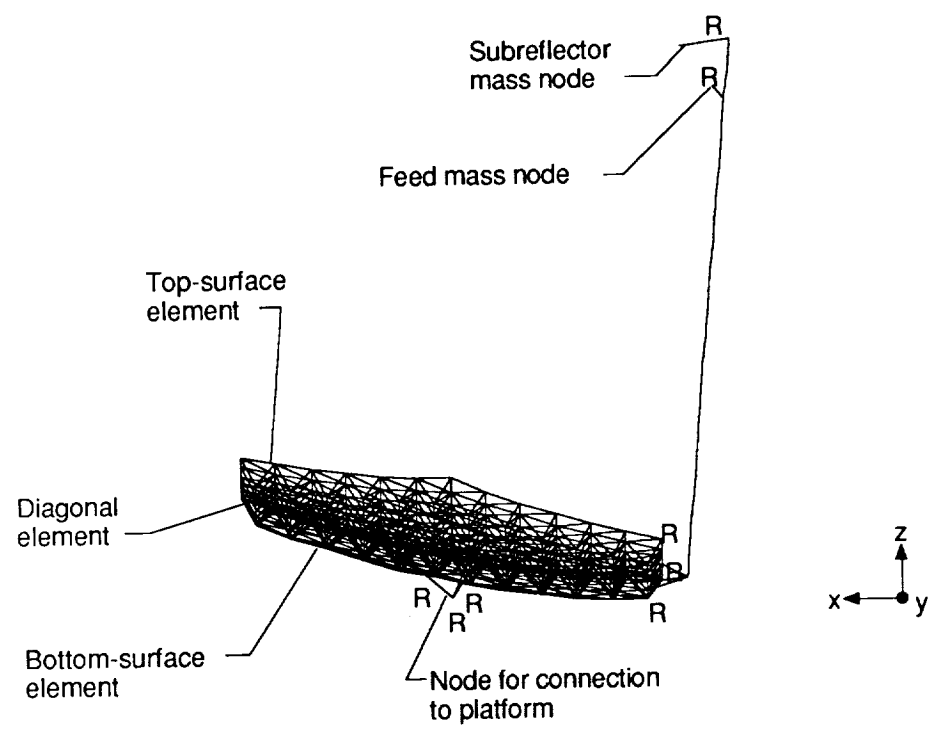
Figure 4. LFMR finite-element model. R denotes a rigid bar.
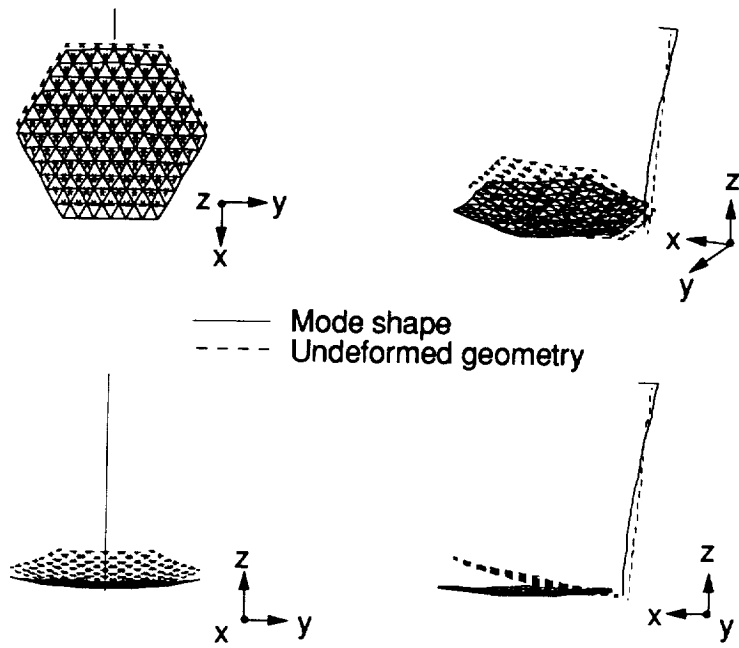
Figure 5. Mode 1 for free-flyer antenna. $f_n = 1.38$ Hz.
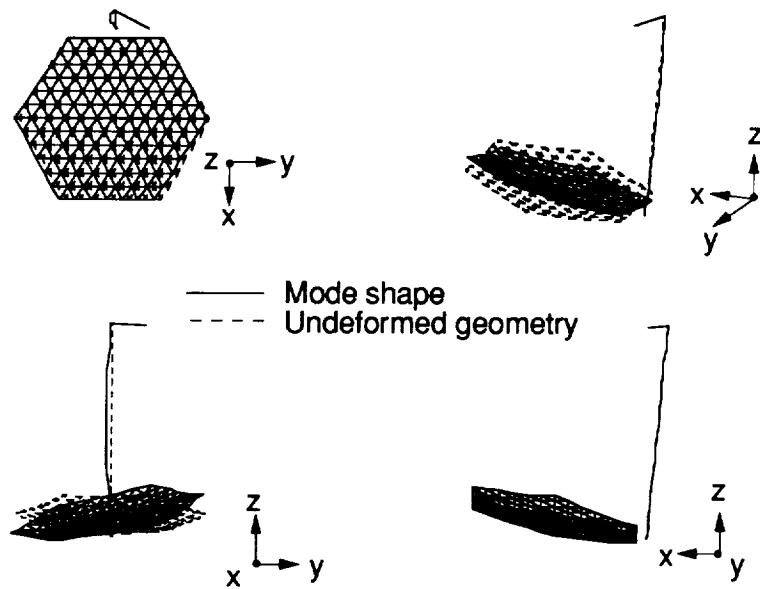
Figure 6. Mode 2 for free-flyer antenna. $f_n = 2.30$ Hz.

20
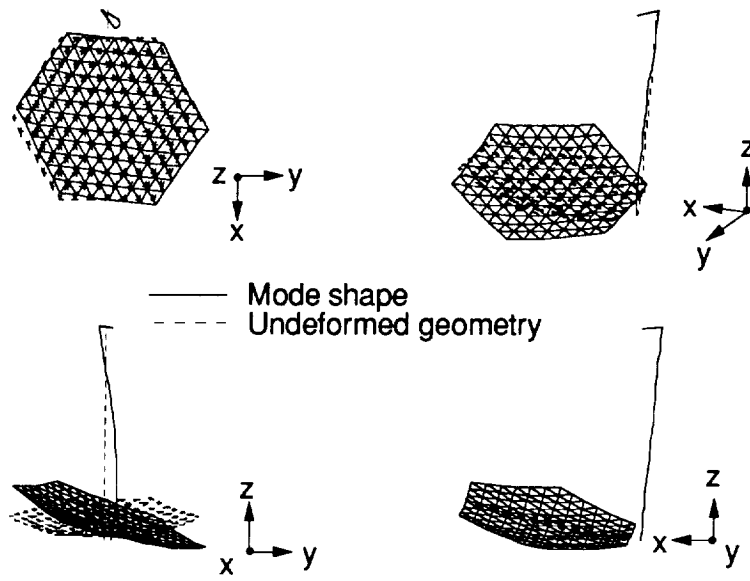
Figure 7. Mode 3 for free-flyer antenna. $f_n = 2.81$ Hz.
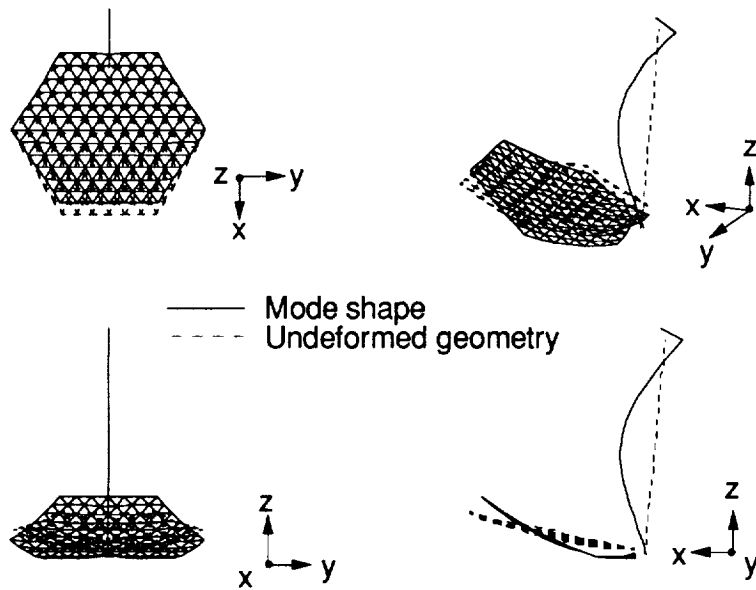
Figure 8. Mode 4 for free-flyer antenna. $f_n = 7.48$ Hz.
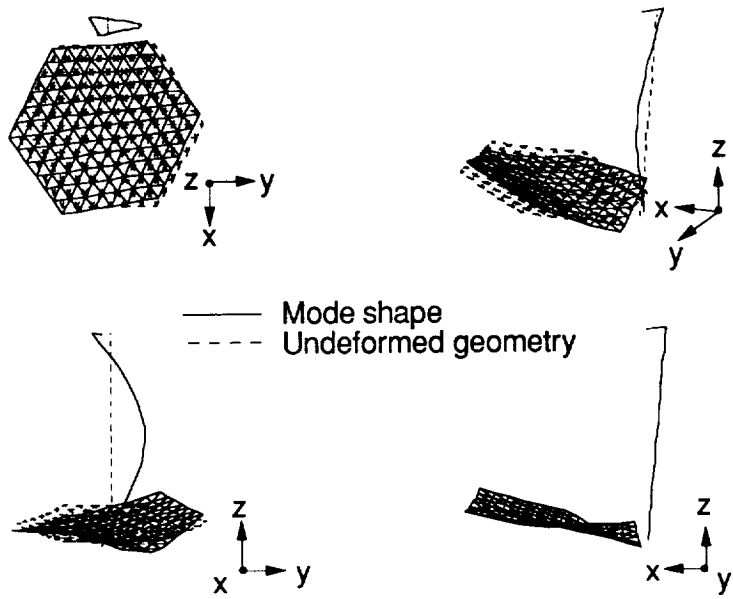
Figure 9. Mode 5 for free-flyer antenna. $f_n = 9.44$ Hz.
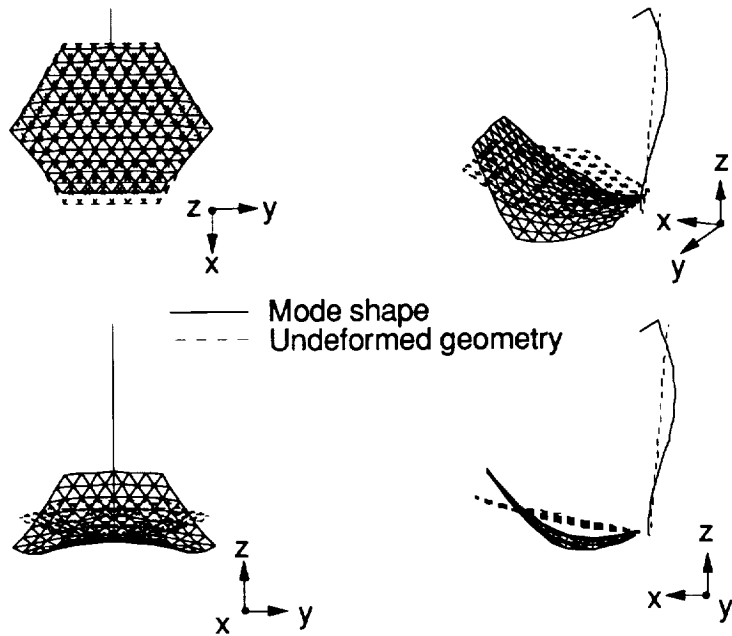
Figure 10. Mode 6 for free-flyer antenna. $f_n = 10.98$ Hz.
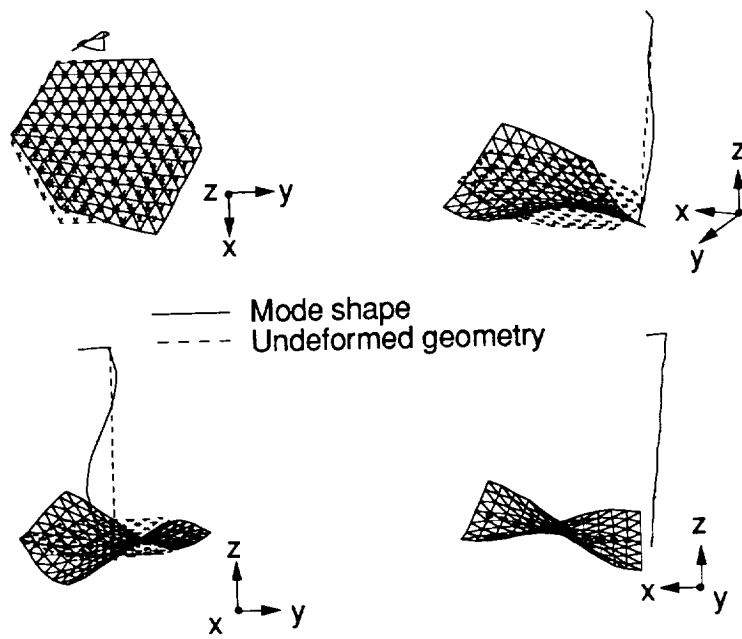
Figure 11. Mode 7 for free-flyer antenna. $f_n = 14.27$ Hz.
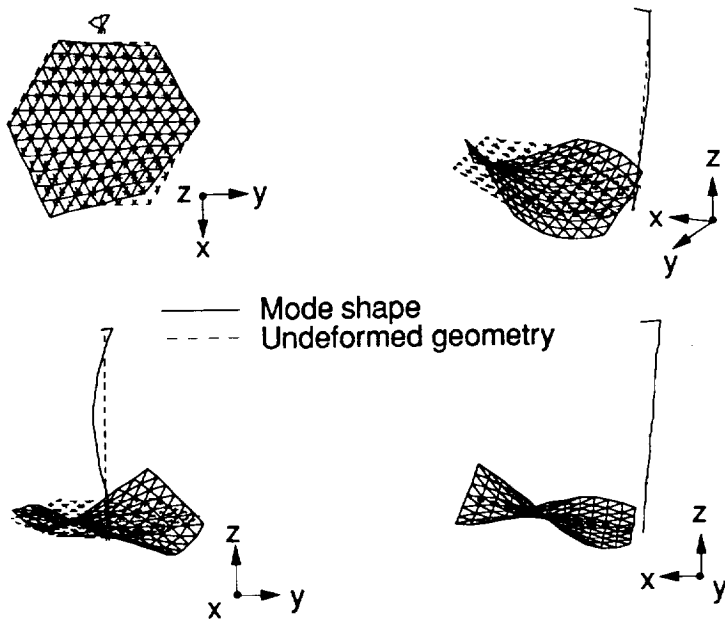
Figure 12. Mode 8 for free-flyer antenna. $f_n = 16.65$ Hz.
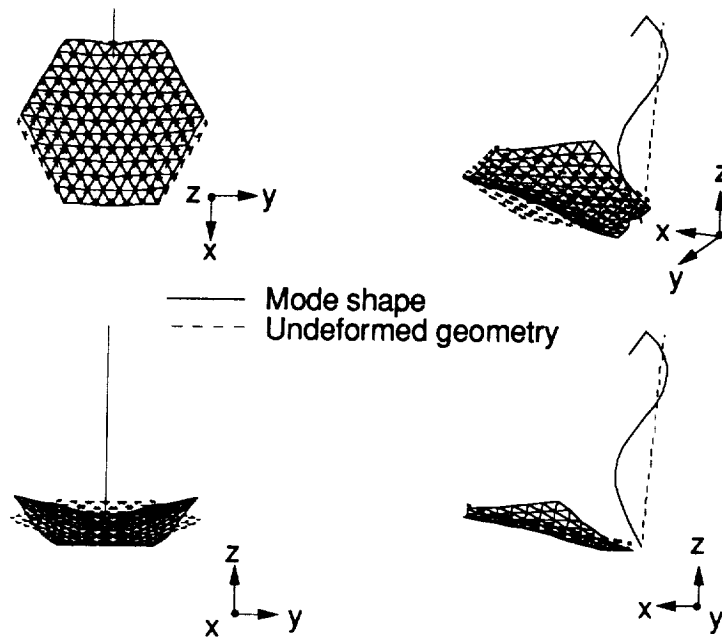
Figure 13. Mode 9 for free-flyer antenna. $f_n = 18.00$ Hz.
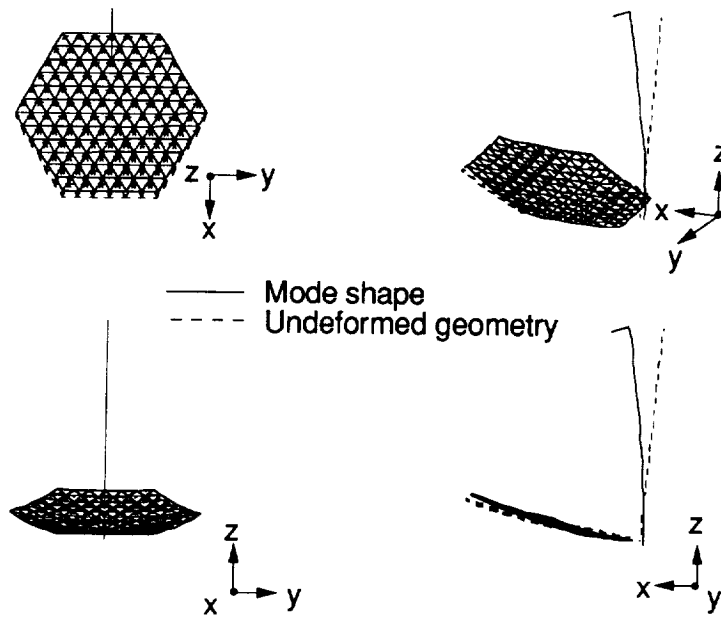
Figure 14. Mode 1 for platform-mounted antenna. $f_n = 0.45$ Hz.
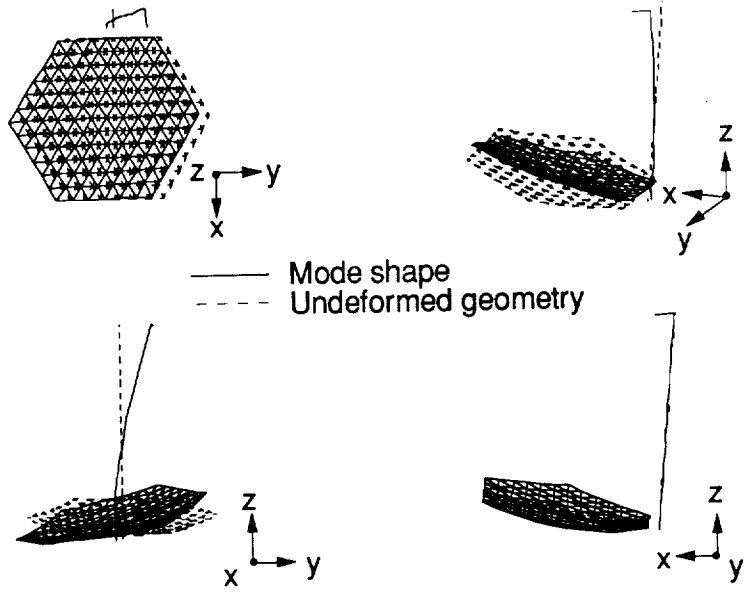
Figure 15. Mode 2 for platform-mounted antenna. $f_n = 0.72$ Hz.
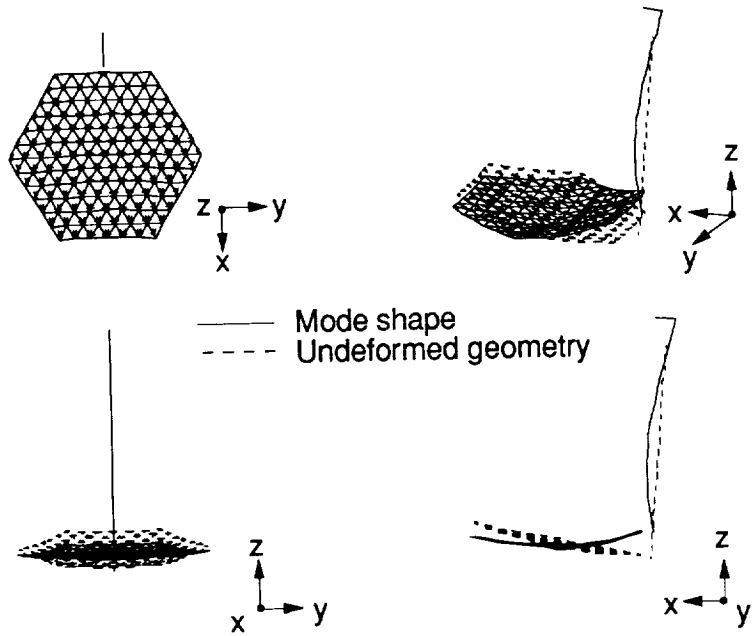
Figure 16. Mode 3 for platform-mounted antenna. $f_n = 2.10$ Hz.

25
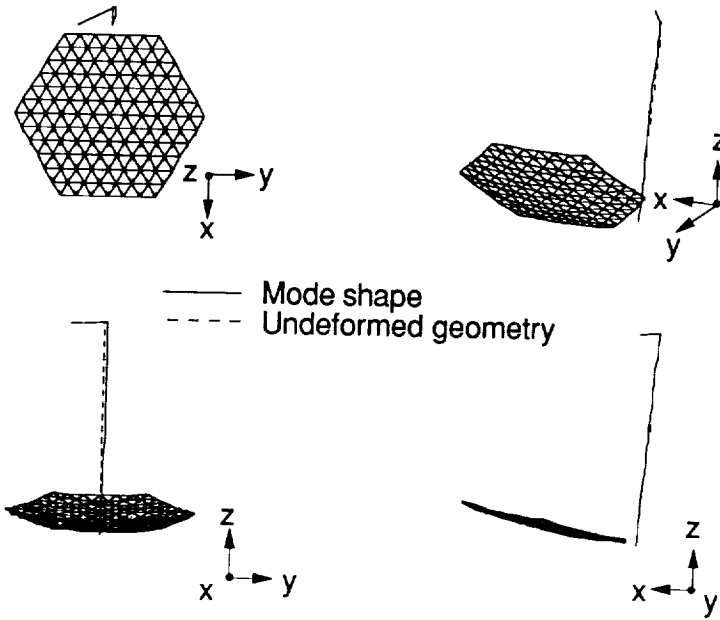
Figure 17. Mode 4 for platform-mounted antenna. $f_n = 2.33$ Hz.
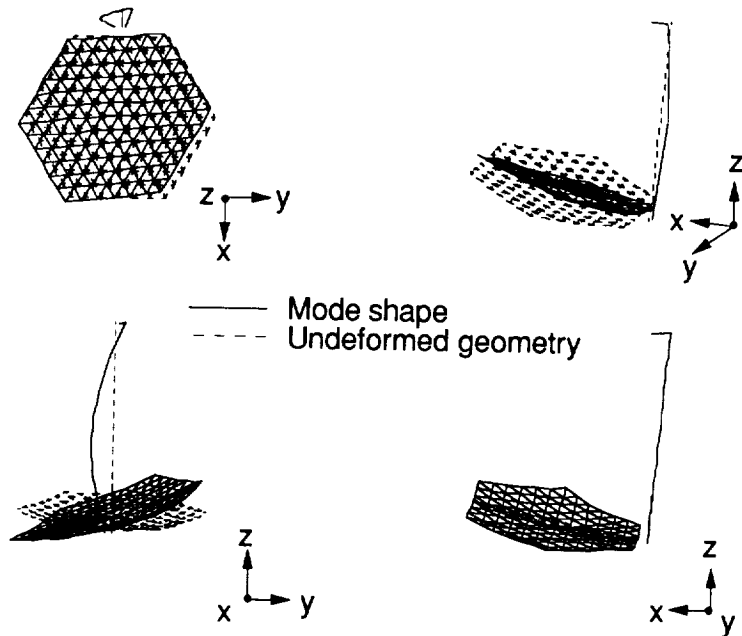
Figure 18. Mode 5 for platform-mounted antenna. $f_n = 6.89$ Hz.

26
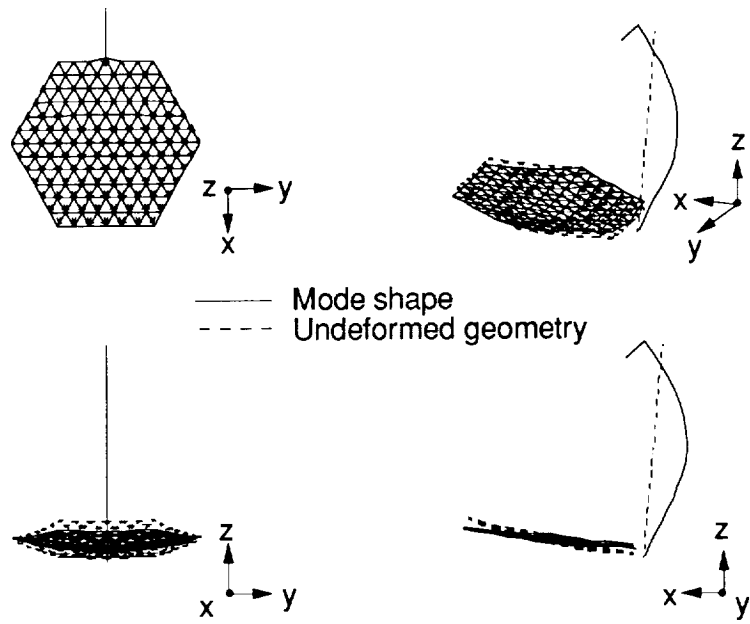
Figure 19. Mode 6 for platform-mounted antenna. $f_n = 7.91$ Hz.
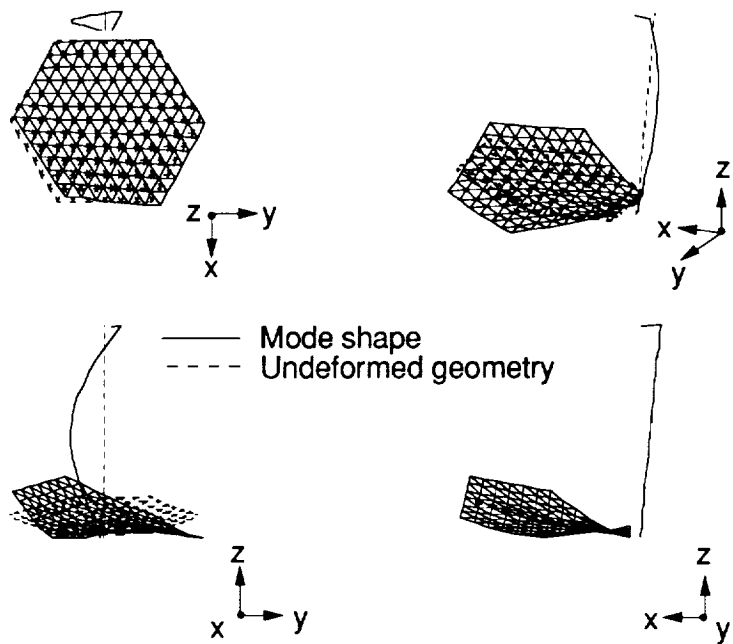
Figure 20. Mode 7 for platform-mounted antenna. $f_n = 8.82$ Hz.
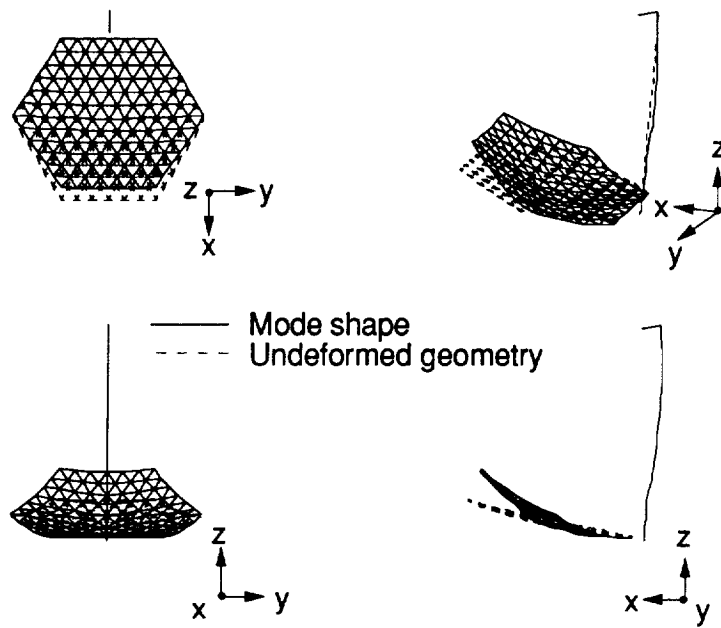
Figure 21. Mode 8 for platform-mounted antenna. $f_n = 10.50$ Hz.
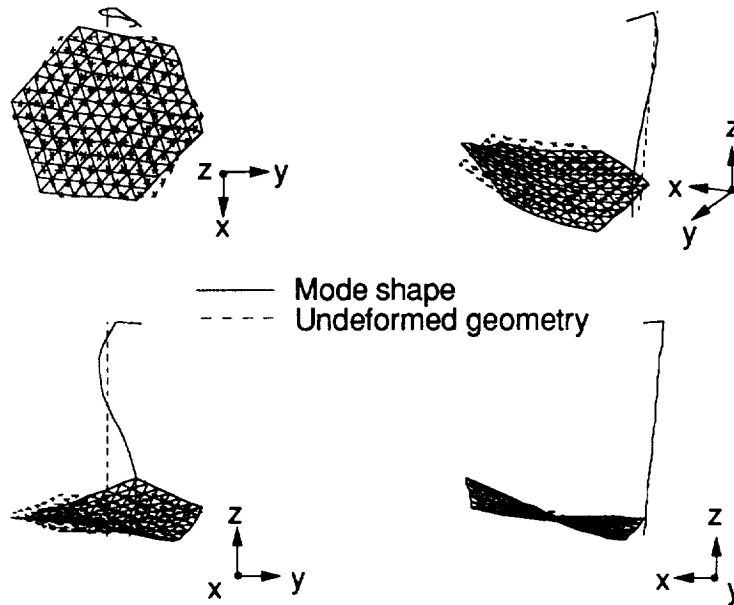
Figure 22. Mode 9 for platform-mounted antenna. $f_n = 13.94$ Hz.

A to G - Full Earth-disk scan
B to F - Individual line scan (Duration = t_ℓ)
B to E - East-west turnaround (Duration = t_{TA})
C to D - North-south step (Duration = t_S)
E to F - Steady motion; no torque (Duration = $t_\ell - t_{TA}$)
G to A - Reset maneuver (Duration = t_ℓ)
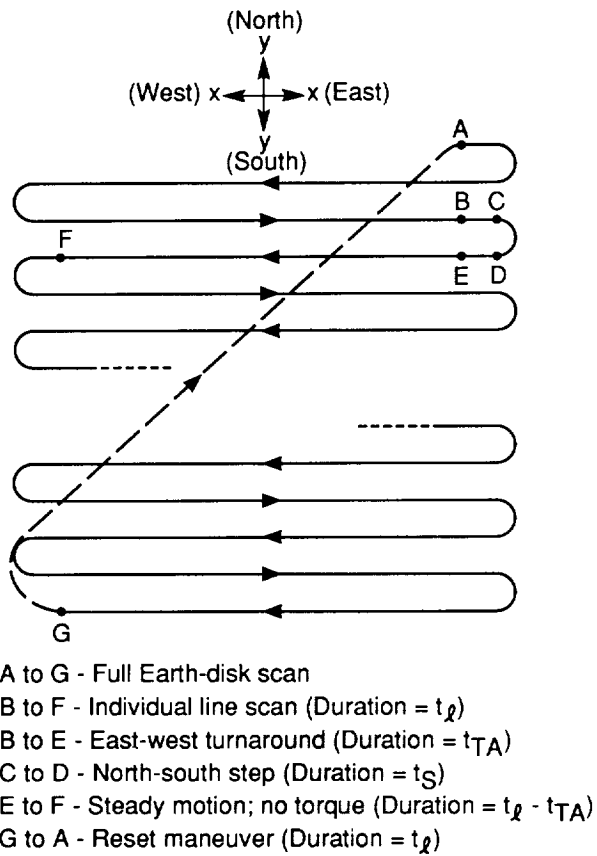
Figure 23. Antenna scan pattern (not to scale).

(a) East - west torque input function.

(b) North - south torque input function.
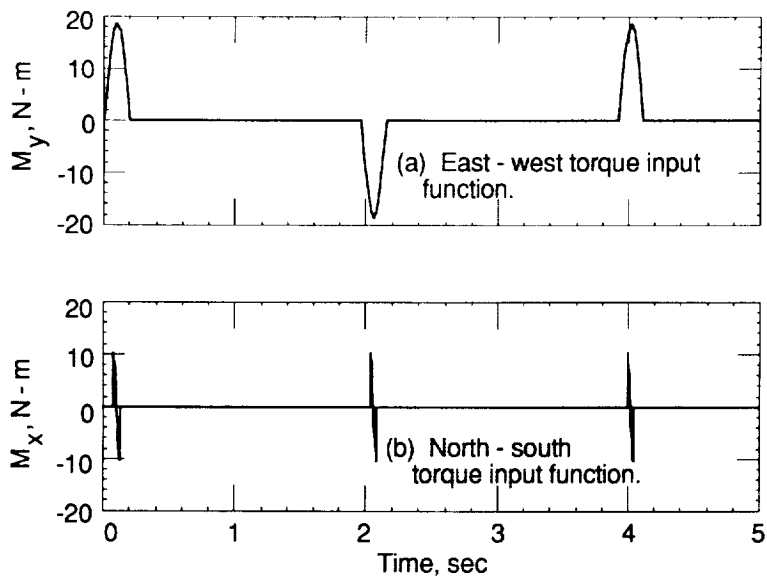
Figure 24. The first 5 sec of scanning torque input functions.

Optimum
pointing
direction

Φ_x

Φ_x

$\Phi_{s,x}$

$\Phi_{s,x}$

$\Phi_{f,x}$

●   Feed/subreflector system
━━━━━ Undistorted antenna
─ ─ ─ ─ Best-fit paraboloid and its axis of symmetry
━━·━━ Distorted feed mast
─ ─ ─ ─► Pointing direction of distorted antenna system

$\Phi_{s,x}$ = Pointing error about x-axis due to surface distortion
$\Phi_{f,x}$ = Pointing error about x-axis due to subreflector
      (i.e., feed mast) displacement
Φ_x = $2\Phi_{s,x}$ - $\Phi_{f,x}$ = Combined pointing error about x-axis

Figure 25. Definition of pointing error.

$\times 10^{-6}$

6.0

4.0

2.0

0

rms surface roughness, m

0   5   10   15   20   25

Time, sec
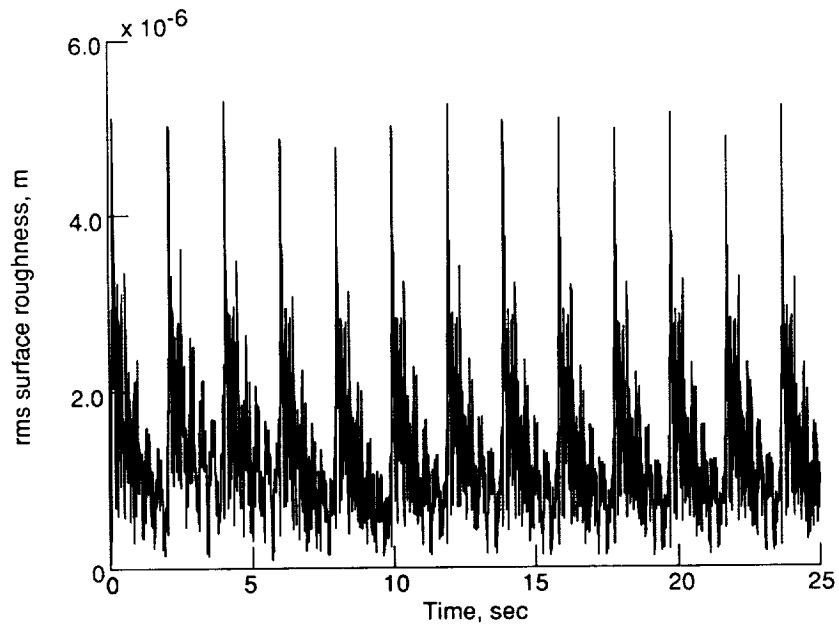
Figure 26. The rms surface roughness for the free-flyer antenna.
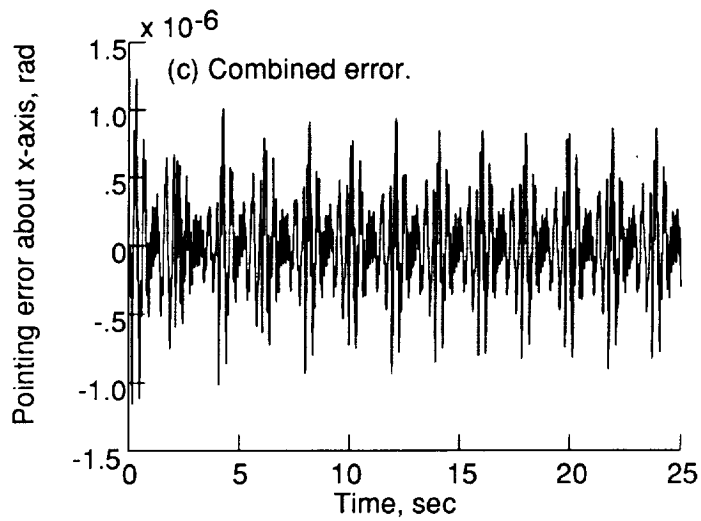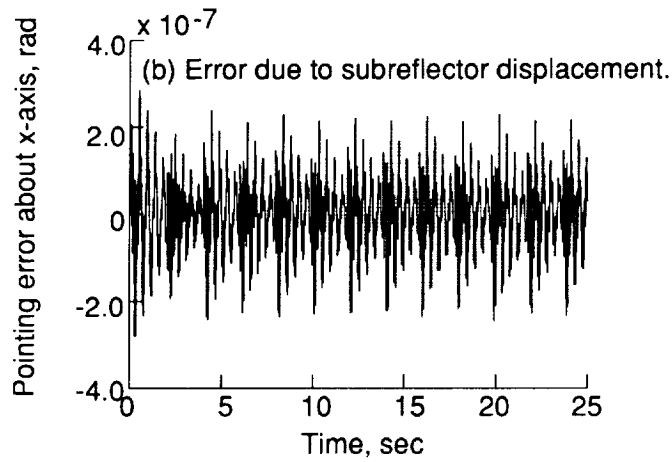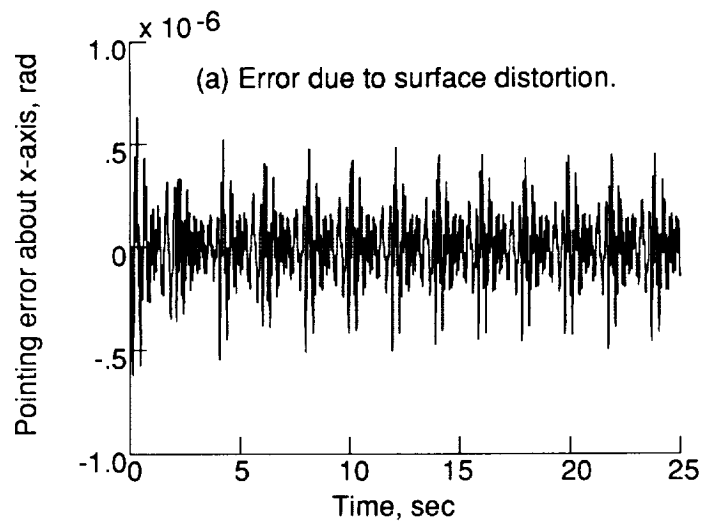
Figure 27. Pointing error about x-axis for free-flyer antenna.
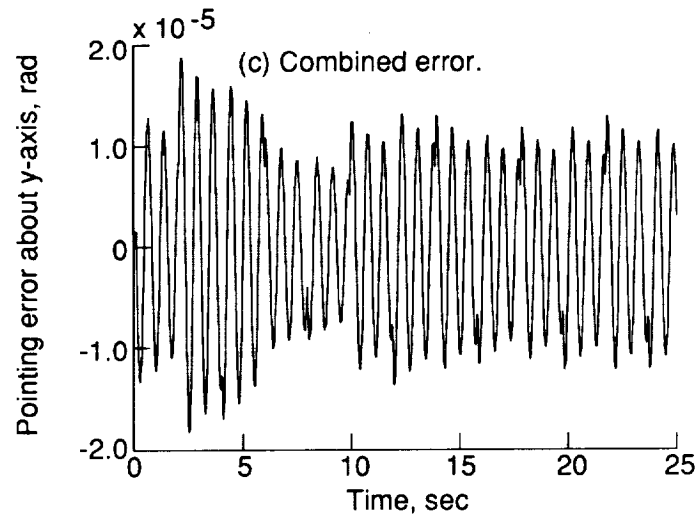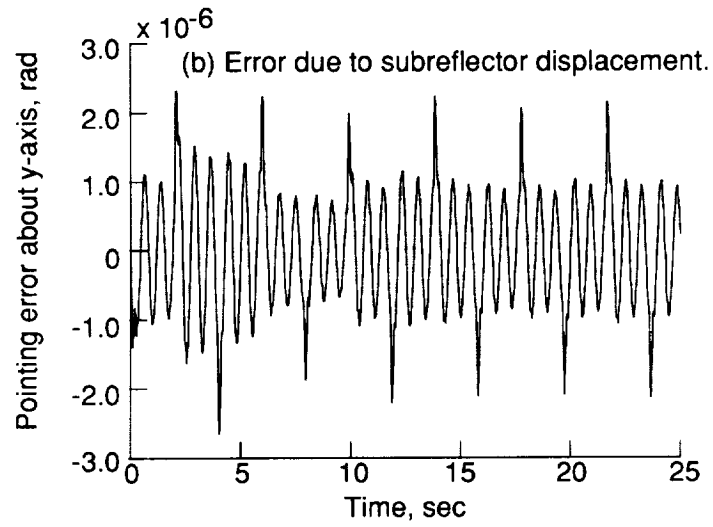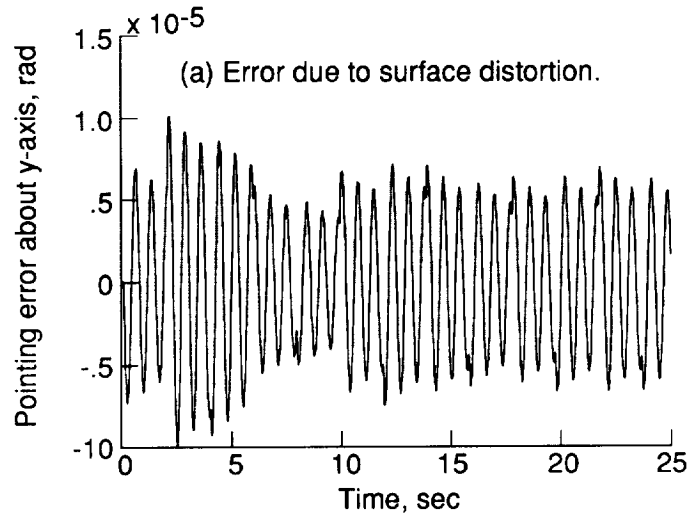
Figure 28. Pointing error about y-axis for free-flyer antenna.
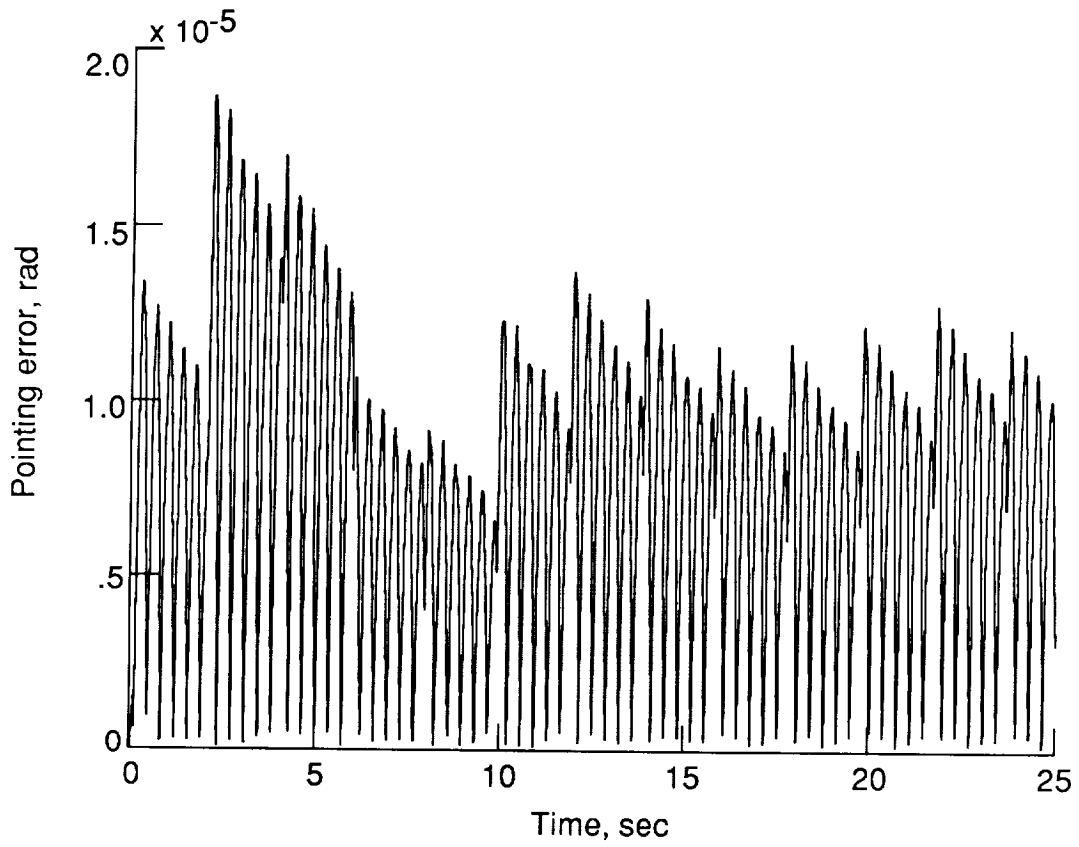
Figure 29. Total LFMR pointing error for free-flyer antenna.

33
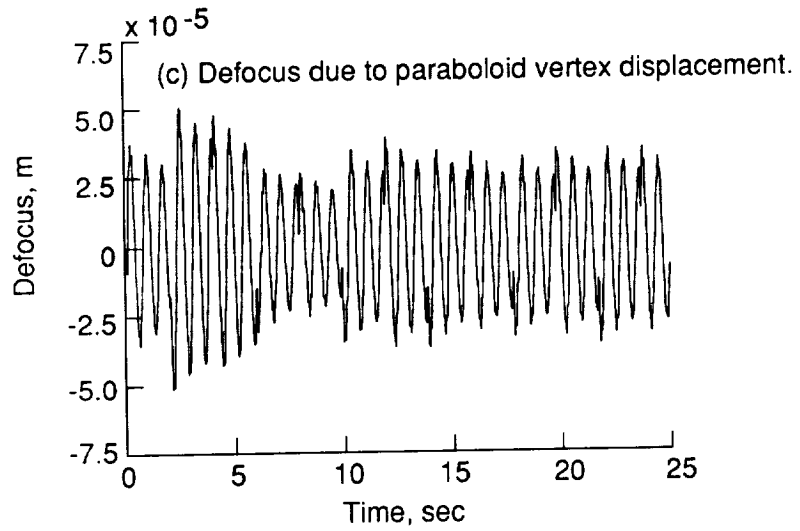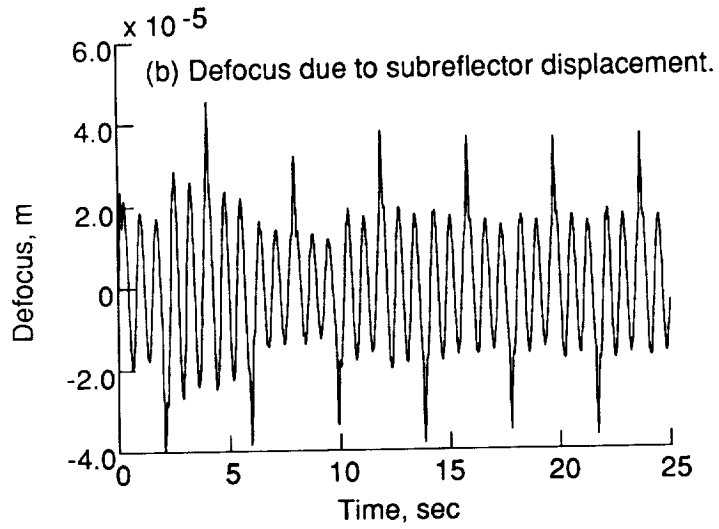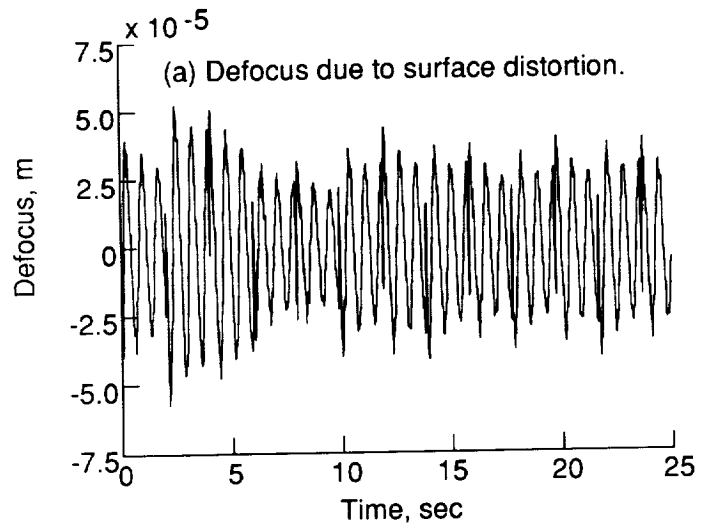
Figure 30. Defocus for free-flyer antenna.
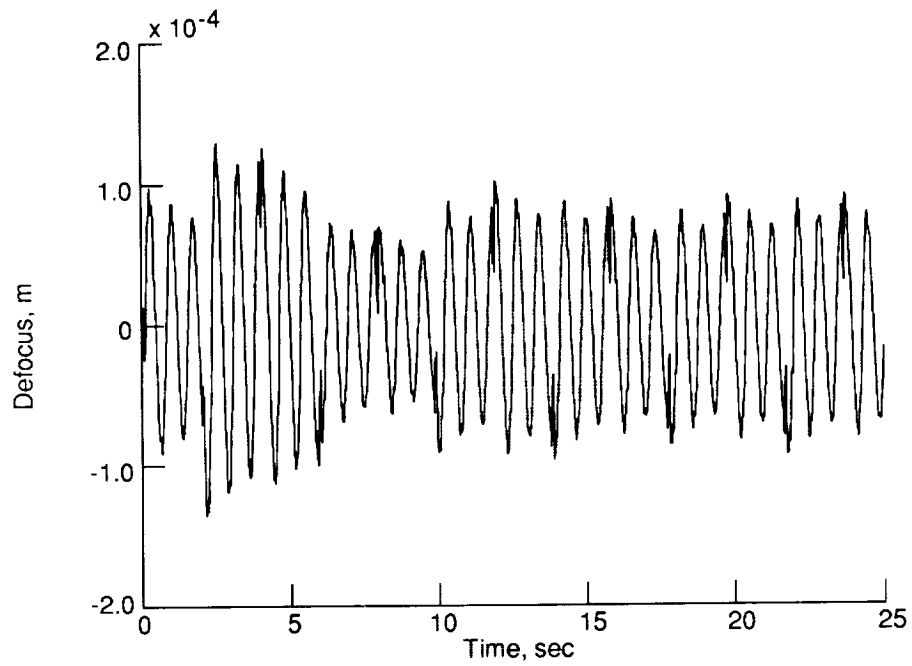
Figure 31. Total LFMR defocus for free-flyer antenna.
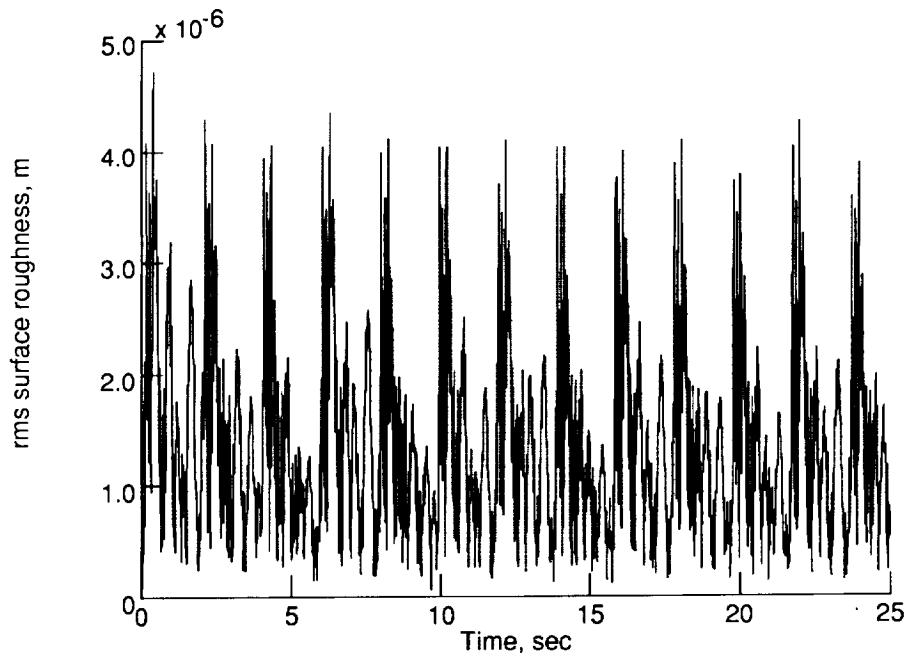
Figure 32. The rms surface roughness for the platform-mounted antenna.
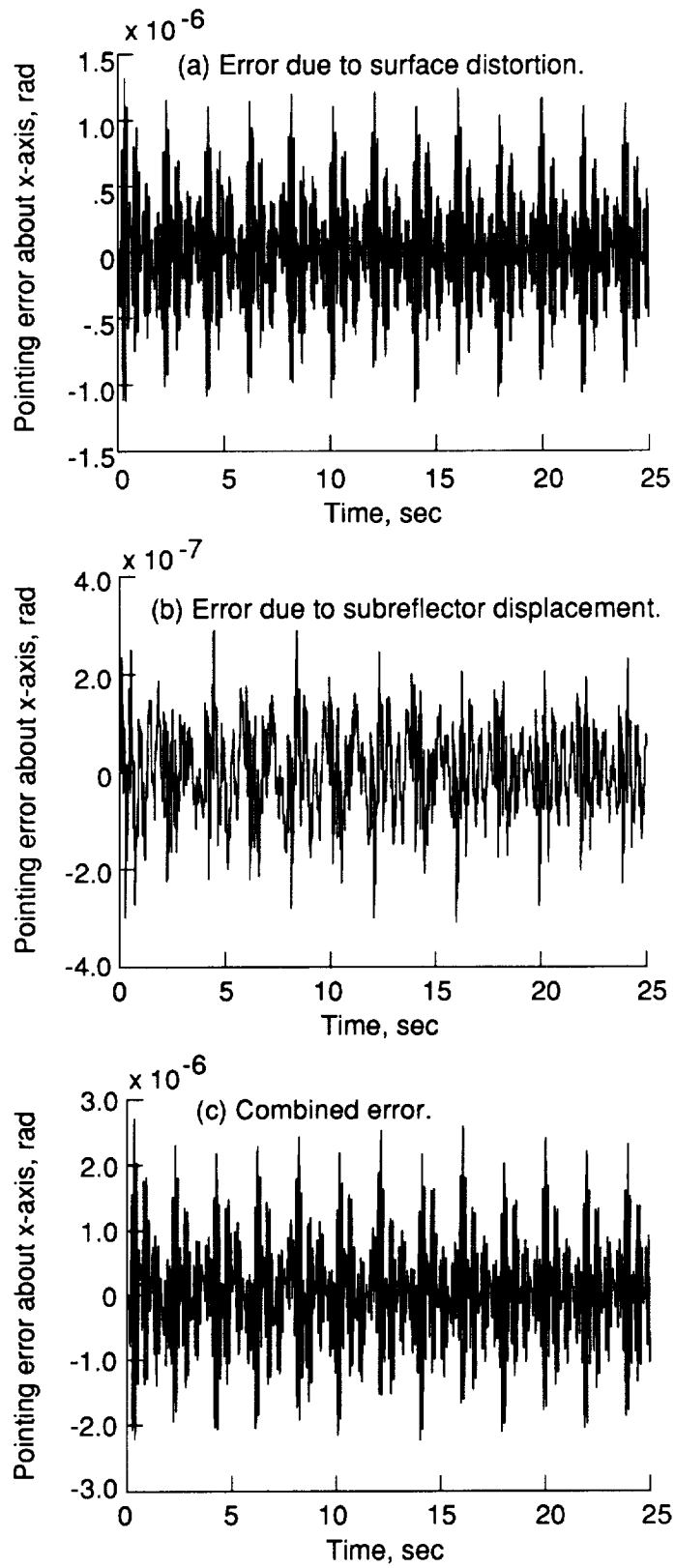
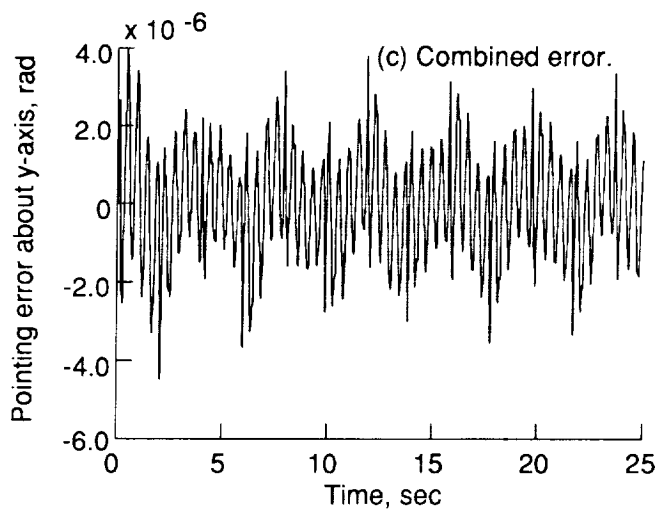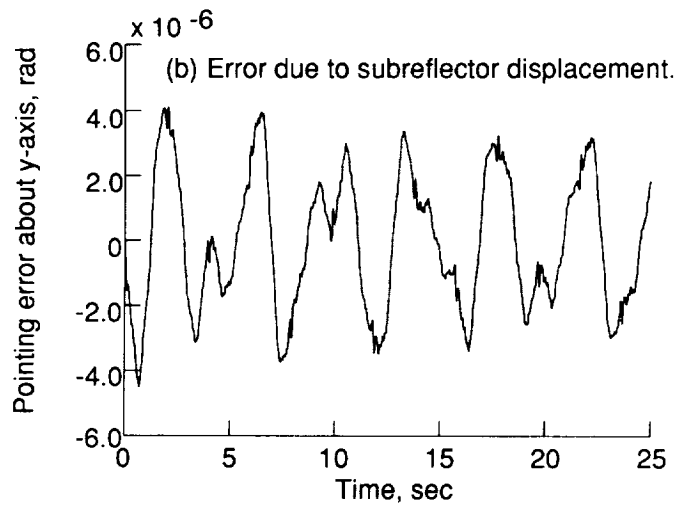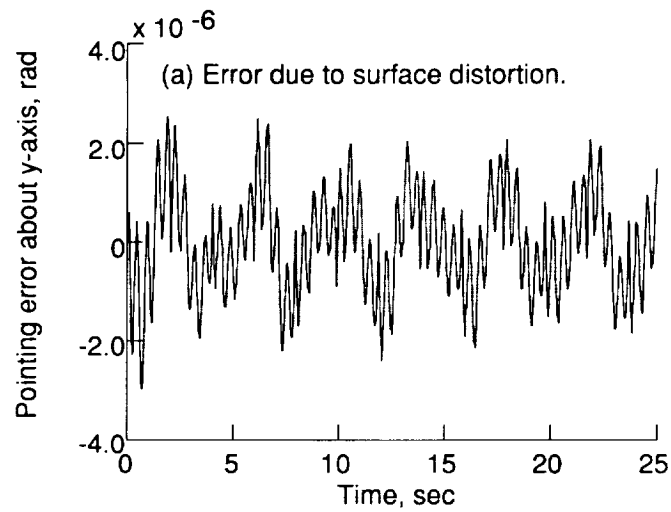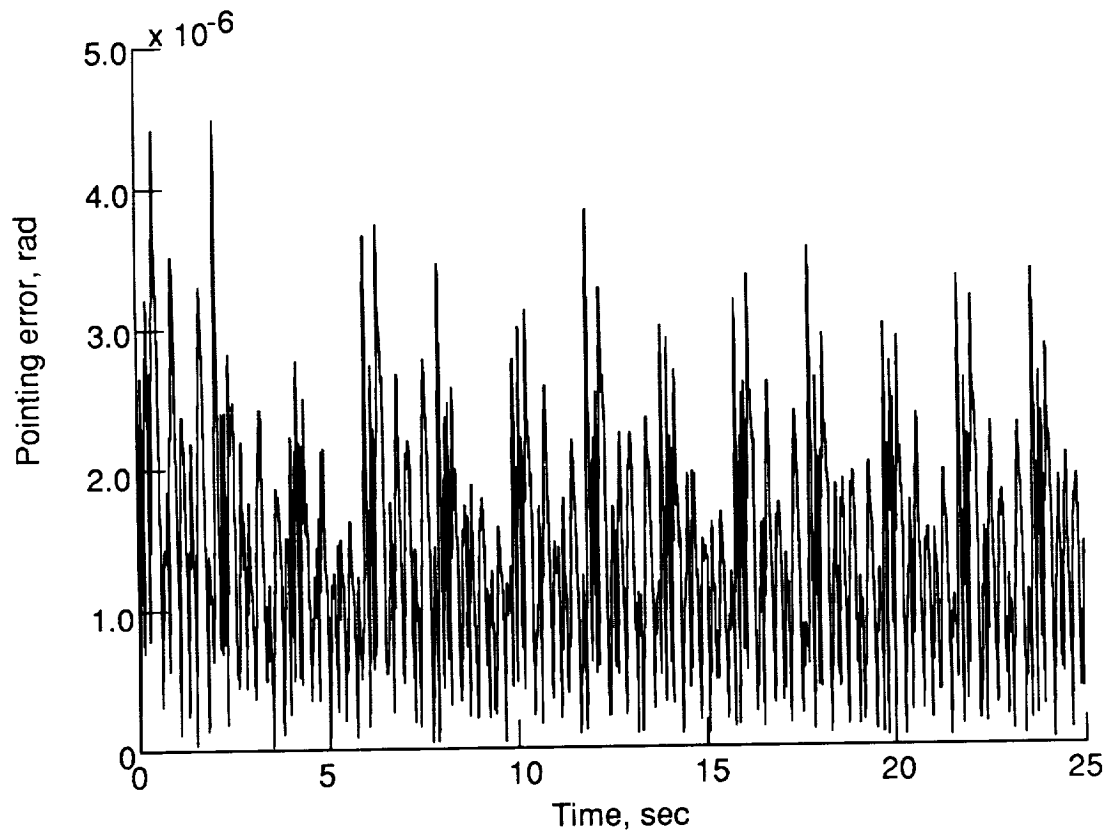Figure 33. Pointing error about x-axis for platform-mounted antenna.

Figure 34. Pointing error about y-axis for platform-mounted antenna.

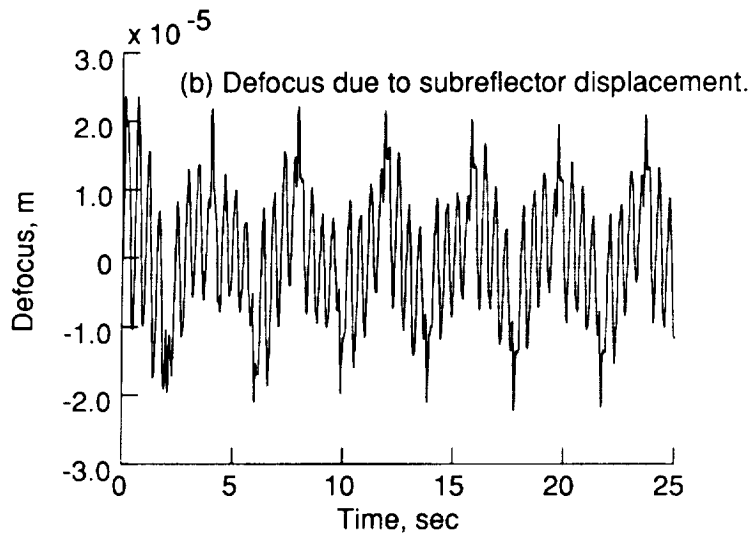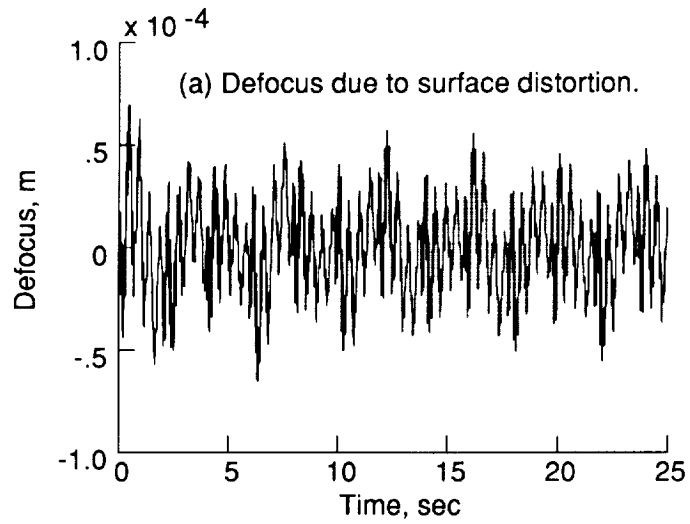Figure 35. Total LFMR pointing error for platform-mounted antenna.
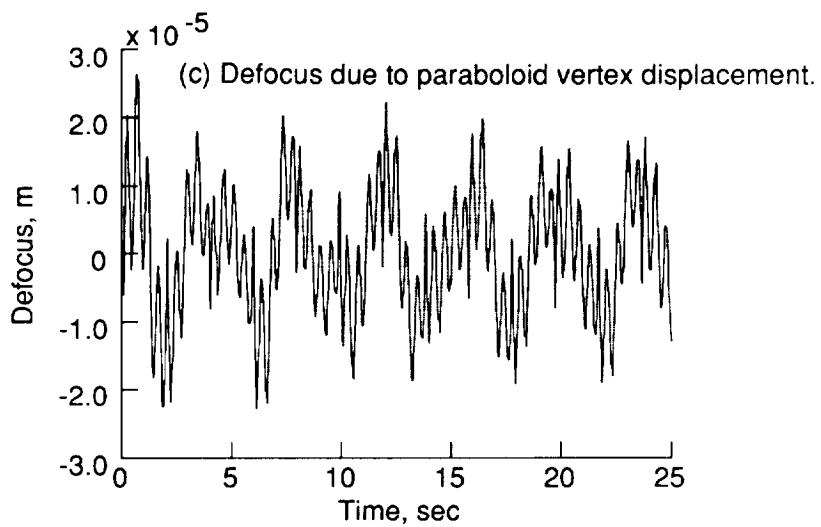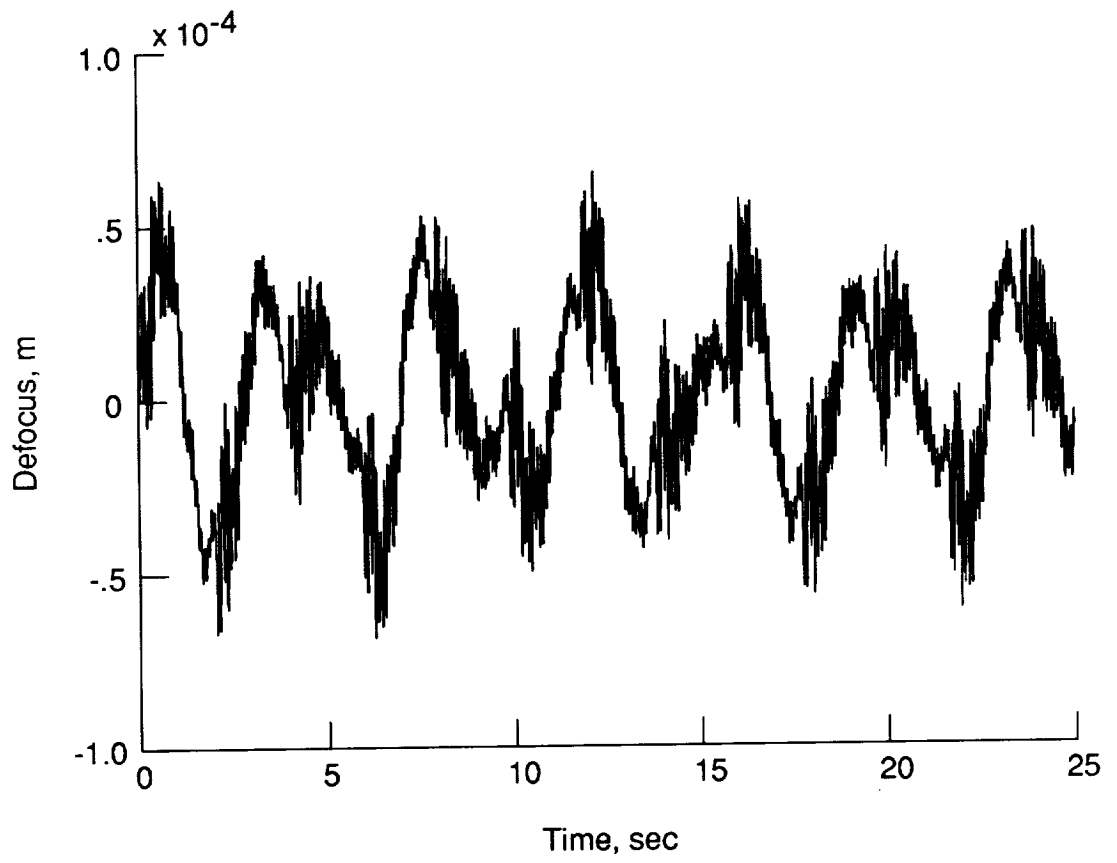
Figure 36. Defocus for platform-mounted antenna.

Figure 37. Total LFMR defocus for platform-mounted antenna.

40

NASA
National Aeronautics and
Space Administration

Report Documentation Page

1. Report No. NASA TP-3041	2. Government Accession No.	3. Recipient's Catalog No.

4. Title and Subtitle	5. Report Date
On-Orbit Structural Dynamic Performance of a 15-Meter Microwave Radiometer Antenna	December 1990
	6. Performing Organization Code

7. Author(s)	8. Performing Organization Report No.
Deborah M. Wahls, Jeffery T. Farmer, and David W. Sleight	L-16795

9. Performing Organization Name and Address	10. Work Unit No.
NASA Langley Research Center Hampton, VA 23665-5225	506-49-21-02
	11. Contract or Grant No.

12. Sponsoring Agency Name and Address	13. Type of Report and Period Covered
National Aeronautics and Space Administration Washington, DC 20546-0001	Technical Paper
	14. Sponsoring Agency Code

16. Abstract

The present paper addresses the on-orbit structural dynamic performance of a microwave radiometer antenna for Earth-science applications. The radiometer is one of the Earth-observing instruments aboard a geostationary platform proposed as part of the Mission to Planet Earth. The paper presents a sequential approach for assessing the ability of an antenna structure to retain its geometric shape subject to a representative onboard disturbance. This approach includes establishing the structural requirements of the antenna, developing the structural and disturbance models, performing modal and forced-response analyses, and evaluating the resulting distortions in terms of the ability of the antenna to meet stringent structural performance requirements. Two antenna configurations are discussed: free-flying and platform-mounted. These configurations are analyzed for a representative disturbance function that simulates rotation of the subreflector during a raster-type scan of the Earth disk. Results show that the scanning maneuver modeled would not induce antenna structural errors outside the specified limits.

17. Key Words (Suggested by Authors(s))	18. Distribution Statement
Geostationary microwave radiometer Antenna structural performance Large space structures Structural analysis Forced-response analysis Computer-aided design and engineering	Unclassified—Unlimited Subject Category 18

19. Security Classif. (of this report)	20. Security Classif. (of this page)	21. No. of Pages	22. Price
Unclassified	Unclassified	41	A03